Applications in Energy and Combustion Science 17 (2024) 100235



Contents lists available at ScienceDirect

Applications in Energy and Combustion Science

journal homepage: www.sciencedirect.com/journal/applications-in-energy-and-combustion-science



Maghemite nanoparticles synthesis via spray flame synthesis and particle characterization by hole in a tube sampling and scanning mobility particle sizing (HIAT-SMPS)

Ricardo Tischendorf [a,b], Orlando Massopo [a,b], Oleg Prymak [c,d], Sophie Dupont [e,f], Fabian Fröde [g,h], Heinz Pitsch [g,h], Reinhold Kneer [e,f], Hans-Joachim Schmid [a,b,*]

[a] Particle Technology Group, University of Paderborn, Paderborn, Germany
[b] Lehrstuhl für Partikeltechnik, Universität Paderborn, Pohlweg 55, 33102 Paderborn
[c] Inorganic Chemistry and Center for Nanointegration Duisburg-Essen (CeNIDE), University of Duisburg-Essen, Essen, Germany
[d] Anorganische Chemie und Center for Nanointegration Duisburg-Essen (CeNIDE), Universität Duisburg-Essen, Universitätstr. 7, 45117 Essen
[e] Institute of Heat and Mass Transfer, RWTH Aachen, Aachen, Germany
[f] Lehrstuhl für Wärme- und Stoffübertragung, RWTH Aachen, Augustinerbach 6, 52056 Aachen
[g] Institute for Combustion Technology, RWTH Aachen, Aachen, Germany
[h] Institut für Technische Verbrennung, RWTH Aachen, Templergraben 64, 52056 Aachen

ARTICLE INFO

Keywords:
SpraySyn2
Spray flame synthesis
Maghemite nanoparticles
Gas to particle-conversion
Hole in a tube sampling

ABSTRACT

In order to standardize spray flame synthesis (SFS) studies, intensive work has been done in recent years on the design of burner types. Thus, in 2019, the so-called SpraySyn1 burner was introduced (SS1), which was subsequently characterized in numerical and experimental studies. Based on this research, a modification of the nozzle design was proposed, which has now been considered in the successor model, SpraySyn2 (SS2). As little is known about the effect of the nozzle adaptation on the particle formation, we operated both burners under identical operating conditions to produce maghemite. The final powder comparison showed that SS2 yielded considerable higher specific surface areas (associated with smaller primary particle sizes), lower polydispersity, and higher phase purity. To obtain further information on the size distributions of aggregates and agglomerates generated by SS2, aerosol samples were extracted by hole in a tube (HIAT) sampling and characterized by scanning mobility particle sizing (SMPS). Samples were extracted along the centerline at different heights above the burner (*HAB*) above the visible flame tip (>7 cm), and quenching experiments were performed to extract the aerosol samples at different dilution rates. Thereby, it was demonstrated that performing detailed quenching experiments is crucial for obtaining representative HIAT-SMPS data. In particular, agglomerates/aggregate sizes were overestimated by up to ~70 % if samples were not sufficiently diluted. If sufficient dilution was applied, distribution widths and mean particle mobility diameters were determined with high accuracy (sample standard derivation <5 %). Our data suggested the evolution of primary particle sizes was mostly completed <7 cm *HAB* and it was shown aggregates/agglomerates present above the visible flame were compact in structure (non-fractal). The mean diameter of the particle ensemble grew along the centerline from 6.9 nm (7 cm) to 11.4 nm (15 cm), while distribution widths grew from 1.42 to 1.52.

1. Introduction

Spray flame synthesis (SFS) represents a promising approach for the fabrication of functional, tailor-made nanoparticles, since it has several considerable advantages over established, competitive liquid phase and gas phase processes [1–3]. In SFS, the precursor is dissolved in an organic, combustible solvent, which is usually atomized by means of oxygen. The emerging spray is subsequently ignited by a self-sustaining gas flame (pilot flame). In principle, particles can evolve by SFS in two different ways [3]. On the one hand, for the gas-to-particle pathway, the precursor transfers to the gas phase, where it reacts into product monomers. Particle formation then takes place via nucleation,

* Corresponding author.
E-mail address: hans-joachim.schmid@upb.de (H.-J. Schmid).

https://doi.org/10.1016/j.jaecs.2023.100235
Received 31 March 2023; Received in revised form 5 December 2023; Accepted 12 December 2023
Available online 14 December 2023
2666-352X/© 2023 The Authors. Published by Elsevier Ltd. This is an open access article under the CC BY-NC-ND license (http://creativecommons.org/licenses/by-nc-nd/4.0/).

agglomeration, sintering and surface growth. On the other hand, for the droplet-to-particle pathway, a fraction of the precursor does not evaporate and rather precipitates/reacts within the liquid feed forming solid precipitates. Since the latter synthesis pathway usually goes ahead with product inhomogeneities (in terms of particle sizes and crystal phases), it is usually desired to avoid it. One material that has been focus of SFS studies in recent years is iron oxide. The research interest in this material is based on two aspects. First, iron can exist in different crystal modifications and oxidation states, which are of technical relevance. For example, fine-scaled maghemite, magnetite and Fe-C particles can be used in medicine and biochemistry due to their superparamagnetic properties [4–7]. And second, iron oxides represent well-studied material systems. Thus, using them as material system can be advantageous.

Based on these motives, the question has been addressed to what extent the particle properties of iron oxides can be manipulated by adjusting operating parameters in SFS. For example, Strobel and Pratsinis studied the impact in changing the global oxygen stoichiometry (Φ) by using a closed combustion chamber [8]. In their study, maghemite was produced at $\Phi < 0.87$. At higher values, reduced phases such as magnetite and wustite were formed due to oxygen limitation. Li et al. also produced maghemite understoichiometrically in their study [9]. However, they additionally varied the spray-to-liquid ratio (*SLR*) to manipulate average primary particle sizes. In this study, the primary particle size as measured by X-ray powder diffraction (XRD) scaled with the *SLR* value over a 2/5-power-law. In another study, Jossen et al. postulated that the dominance of the droplet-to-particle pathway can be controlled by manipulating the relative precursor volatility (R_T) and the specific flame enthalpy (*H*) [10]. From physical point of view, the model of this study described that the precursor (which is usually a solid material at room temperature) remains as residual in the droplet if its melting/decomposition temperature is lower than the boiling temperature of the solvent, while low specific flame enthalpies are present at same time. Some studies such as those by Grimm et al. [11,12], Alkan et al. [13], and Carvajal et al. [14] have also evaluated the purity of synthesized iron oxides. Those studies presented that product impurities can form in SFS, with surface adsorbates and carbon particles/coatings being the most prominent ones.

Even though existing studies have already provided interesting insights into the particle formation in SFS, quite little attention has been paid to the burner configuration. Note, the studies mentioned above used different burner configurations in most cases, unfortunately limiting their comparability. And in fact, recent studies have increasingly shown that the burner/nozzle configuration has a dominant role in SFS. For example, Sorvali et al. operated two burner configurations at similar global oxygen stoichiometry, Φ [15,16], and it was demonstrated phase compositions can be considerably affected by the burner type and the flow configuration. Furtheremore, Bieber et al. demonstrated primary particle sizes can be affected by up to 30 % if nozzle geometries are changed slightly (while maintaining the burner flow rates constant) [17]. Carvajal et al. further showed that carbon depositions can evolve as impurity even at high global oxygen excess [14], which is in contradiction to the study of Strobel and Pratsinis [8] at first glance. However, this discrepancy in literature also highlights the relevance on taking the burner configuration into consideration, rather than operating conditions only. Due to the obvious necessity to standardize SFS experiments, work has been done in the past decade on the design of standard burners. Thus, in 2019, Schneider et al. introduced the SpraySyn1 burner (SS1) [18], which was subsequently used in a large joint research program resulting in numerous experimental [19–37] and numerical studies [38–49]. Subsequently, it was revealed that SS1 leads to slight flame pulsations (temporal flucatuations in the flame activity). Those pulsations take place in the lower single digit ms-regime, and are caused by an aperiodic atomization and ignition of larger liquid lumps entraining into the pilot flame. To produce a more homogeneous spray flame, alternative nozzles were employed by Bieber et al. and Karaminejad et al. [17,23]. Based on the revision of the nozzle geometry, a second standard burner, the SpraySyn2 burner (SS2), has been proposed.

To the best of our knowledge, it has not yet been investigated to what extent the adjustment in design from SS1 to SS2 can affect final particle properties in detail. For this reason we generated iron oxide particles by operating both burner types at identical operating conditions, and final particle properties (structure, phase composition, purity) were compared. A precursor mixture of iron (III) nitrate (INN) dissolved in ethanol (EtOH) and 2-ethylhexanoic acid (2-EHA) was used, representing a common precursor composition in literature [15,16,18,37,50].

As information about the particle structure evolution of iron oxides using SS2 are still rare, we additionally extracted aerosol samples from the corresponding flame centerline at various height above burner (*HAB*) positions above the flame tip. The aim was to investigate local *in situ* size distributions of agglomerates and aggregates. Therefore, aerosol samples were extracted using a hole in a tube (HIAT) probe, and were subsequently characterized using scanning mobility particle sizing (SMPS). At each *HAB* so-called quenching experiments were performed (implying the probe dilution ratio (*DR*) was manipulated stepwise). This way, at high *DR*, steady-state values for average mobility sizes and size distribution widths were derived, and the impact of adapting *DR* was quantified. Although HIAT probes have been used for some SFS experiments in the past [21,51,52], authors tend to show only final, representative data. And hence, unfortunately, specific challenges and requirements for performing correct quenching experiments in SFS are still rare. For this reason, we show and discuss data sets obtained from our quenching experiments in detail, and we highlight special issues one has to face using HIAT probes in SFS approaches.

At this point, we also want to emphasise that the term *in situ* is used here in a sense that we aim to characterize the particles as the are in the original, undisturbed flame. Since sampling always implies some disturbances (e.g., flow and temperature distribution) and transport might further modify the sample, this aim can never be achieved completely. However, we extensively discuss in this paper, how a strong bias caused by aggregation can be avoided by proper dilution. In fact, even non-intrusive optical methods typically show their own biases and are therefore also not capable of determining absolute *in situ* characteristics. Therefore, we used the term ‚*in situ* characterization' as an aim, which can not be achieved fully but to a large extent even for intrusive sampling techniques like HIAT sampling, if proper conditions are maintained.

2. Material and methods

In our study, iron oxide particles were prepared by processing a precursor mixture known from literature with two standard burner types (SS1 and SS2). Necessary basics about burner and precursor components used are presented in *chapter 2.1*. A brief analytical description of the SFS experiments is presented in *chapter 2.2*. There, images of both spray flames are compared. *Chapter 2.3* explains how powder samples were collected and analysed. For the SFS using SS2, *in situ* data of local particle size distributions were obtained by using a HIAT-SMPS coupling. The necessary fundamentals for those *in situ* measurements are presented in *chapter 2.4*. Detailed information about material and methods can also be found on SpraySyn.org (open access database).

2.1. Burner types, operating conditions, precursor composition

As mentioned, SS1 and SS2 were used as burner types. The basic design of SS1 was described in 2019 by Schneider et al. [18]. Both burners use an identical porous sinter matrix to provide a sheath flow and the pilot flame gases. Hence, the main difference represents the central nozzle which is utilized for the liquid feed atomization (see Fig. 1). Both burners have in common that the capillary (which delivers the liquid feed) can be positioned precisely by three micrometer screws. As shown for SS1, very rotationally symmetric flames can be achieved

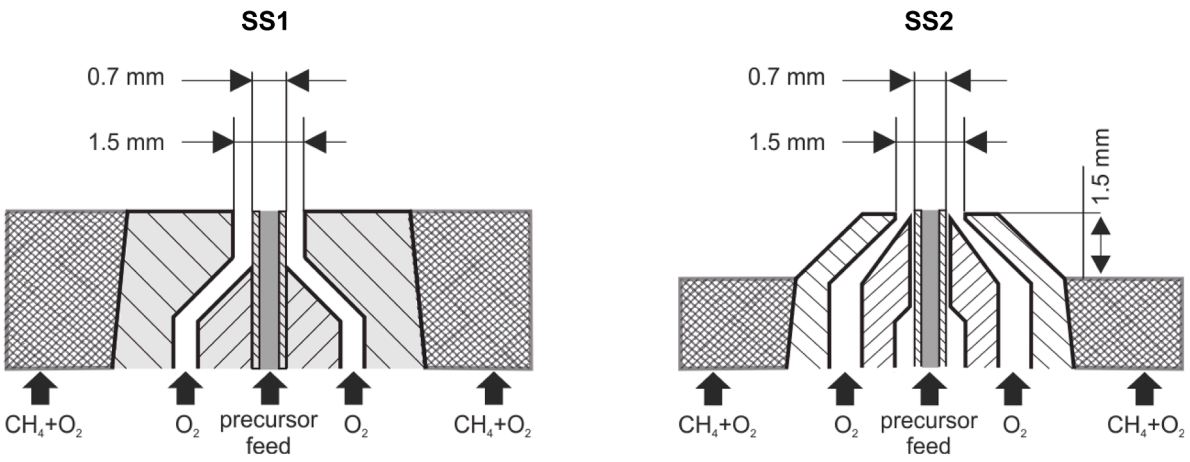

Fig. 1. Comparison of nozzle geometries of SS1 and SS2. $\mathbf{O_2}$ is used as dispersion gas, $\mathbf{CH_4}$+$\mathbf{O_2}$ as pilot flame gas mixture.

this way [18]. The characteristics of SS1 have been investigated in recent years by a number of experimental and numerical studies. Two studies revealed SS1 flames can exhibit pulsations in the millisecond range [17,23]. Those fluctuations arise because the precursor feed is atomized aperiodically (caused by the fact the capillary and the dispersion gas line are aligned in parallel yielding a 'barrier effect' between the pilot flame and the liquid feed). To counteract this effect, an inclination of the dispersion gas line relative to the capillary was proposed [17,23]. This angling provided a homogenization of the flame activity over time and was in consequence the major innovation in the SS2 design. In our experiments, both burner types were operated with identical operational parameters (Table 1). The liquid feed was delivered by a continuously operating syringe pump (KDS Gemini 88 Plus, KD Scientific Inc.) while gas flows were controlled by mass flow controllers (Bronkhorst High-Tech B.V.). All synthesis were operated in an open combustion chamber. To generate iron oxide particles predominantly by the gas-to-particle conversion, 0.2 M iron (III) nitrate nonahydrate (INN) dissolved in a 35:65 mixture (v/v) of ethanol (EtOH) and 2-ethylhexanoic acid (2-EHA) was used as precursor composition. At this point, it must be emphasized that the use of 2-EHA is well established in the literature, as its presence suppresses droplet-to-particle pathways. In particular, if one would use precursor compositions consisting solely INN and pure alcohols (omitting 2-EHA), large particles >100 nm would evolve from the droplet phase [3,15,16,37,50]. According to the current knowledge, the evolution of those large-sized particles is caused by iron hydrolysis mechanisms forming poor soluble iron hydroxide precipitates, which takes place for several INN-alcohol combinations already at room temperature after a few hours [53,54]. As shown by Meierhofer et al., Stodt et al., Angel et al., and Strobel et al., ester formation and carboxylations take place in precursor solutions if 2-EHA is present [50,53,55–58], which apparently contributes to the stabilization of the Fe-ions against hydrolysis/precipitation.

2.2. Analytical parameters and flame structures

As mentioned, some analytical parameters were discovered in the literature influencing processes in the flame, with H, R_T, Φ, SLR and f_v being most important ones. These parameters are derived from analytical calculations taking into account the burner flow rates, and physical properties of precursor components. So, by definition, they are independent of the burner type. The parameters H and R_T denote the specific flame enthalpy and the relative precursor volatility, respectively. They were used by Jossen et al. to estimate the droplet synthesis pathway of some material systems [10]. In this regard, R_T is defined by physical properties of the precursor mixture, while H is obtained from the reaction balance. Adapting the global oxygen stoichiometry, Φ, was adressed in a bandwidth of studies and is also alterted by the reaction balance. The parameter f_v describes the global volume fraction occupied by particles in the gas phase [59]. To calculate this parameter, the density of the final particle material must be taken into account in addition. The SLR parameter describes the ratio of liquid feed to dispersion gas at standard conditions [9].

Table 2
Analytical parameter set used.

parameter	value
R_T / -	rises *in situ* from 1.14 to 1.56
Φ / -	0.2623
H / kJ g^{-1}_{gas}	3.101
f_v (@2000 K)/ -	3.029×10^{-8}
SLR / mL L_N^{-1}	0.2

To allow a comparison of our SFS experiments, we have summarized the corresponding parameter set in Table 2. Note, due to the parameter's definition, values are independent to the burner type. And since we operated both burner with identical operating conditions, solely one set is provided. For calculating the reaction balance, we assumed that dispersion gas, pilot flame gases, and liquid feed mix up and oxidize completely (forming H_2O, N_2, CO_2, Fe_2O_3). Used chemical reaction equations and mass flow rates are shown in Table S1. Note, to calculate R_T, the boiling temperature of the solvent mixture must be known, which was estimated by using Raoult's law. Also note, based on the very different vapour pressure curves of EtOH and 2-EHA, EtOH should preferentially evaporate from the droplet phase. Hence, 2-EHA concentrates in the droplet, yielding an increase of R_T *in situ*. The vapour pressure curves of 2-EHA and EtOH including the boiling diagram of

Table 1
Utilized burner operating conditions and gas types (gas flow rates at IUPAC standard conditions).

dispersion gas	liquid feed	pilot flame gases		sheath gas
O_2	0.2 M INN in EtOH+2-EHA	O_2	CH_4	air
10 L min^{-1}	2 mL min^{-1}	2 L min^{-1}	16 L min^{-1}	120 L min^{-1}

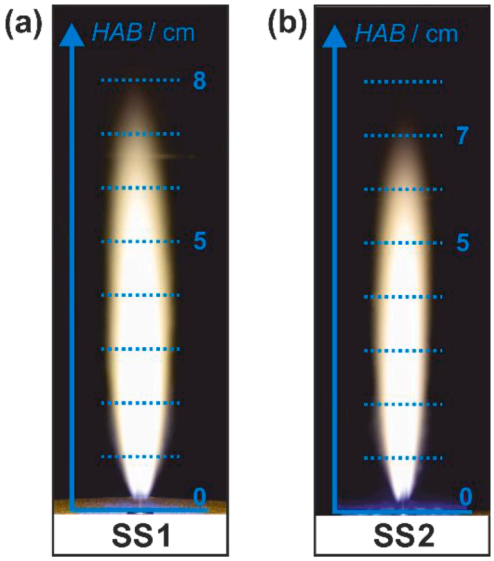

Fig. 2. Comparison of single-lens reflex images for SS1 (a) and SS2 (b) operated at identical operation conditions.

binary EtOH+2-EHA mixtures are shown in Fig. S1. For the calculation of f_v, a particle density of 4.88 g cm^{-3} (maghemite) was used, and the volume expansion of the flame aerosol was calculated according to ideal gas law.

Fig. 2 shows images of both experimental flames (recorded by single-lens reflex camera). Although both burner types were operated with identical flow rates, evolved flame structures differed slightly. In particular, the SS1-flame appeared wider and higher than the SS2-flame. Hence, the positions of the flame tips differed slightly (~8 cm for SS1 vs. ~7 cm for SS2). The differences in flame structure must be attributed to differences in atomization characteristics. Karaminejad et al. have shown that angling the dispersion gas piping results in droplets with smaller diameters, higher velocity, and narrower distribution close to the nozzle [23], which could result in an overall faster evaporation and a less expanded flame geometry for SS2.

2.3. Powder characterization

Particles fabricated by SS1 and SS2 were collected by surface filtration and subsequently analysed in terms of structure, phase and purity by Raman spectroscopy, Brunauer-Emmet-Teller physisorption (BET), XRD, and Attenuated Total Reflection Fourier Transform Infrared Spectroscopy (ATR-FTIR). For this purpose, the generated aerosol was extracted by a vacuum pump (Mink MM 1144 BV, Dr.-Ing. K. Busch GmbH) at 22 cm *HAB* through the fume hood. The aerosol was then directed in a 1 m DN40 metal pipeline toward a surface filter (ePTFE membrane, $R + B$ Filter GmbH). Taking into account the volume flow rate of the pump (~60 m^3 h^{-1}), the residence time from the point of extraction to the surface filter was ~75 ms in our setup. The aerosol cooled down considerably during its advection, which prevented changes of particle properties on the filter (caused by excessive temperatures). By thermocouple we measured values in the range of 100–150 °C close to the membrane. And as phase transformations and sintering of iron oxides occur at much higher temperatures, this temperature range was sufficient for the material system of our experiments. For example, the hematite-maghemite transfer takes place at >400 °C [60,61]. Also, iron hydroxides which could potentially be formed via a droplet synthesis route would only transform at higher temperatures, i.e., in the range of 200–300 °C [60,61].

Raman spectroscopy was used for phase identification and was conducted via an inVia™ confocal Raman microscope (Renishaw plc.). A low laser intensity of 1 % at 633 nm (0.175 mW) was utilized. Note, according to Hanesch et al. [62], we also tested higher relative laser intensities. However, they coincided with a maghemite-hematite phase transformation. By performing 50 repetitions (10 s each) a single measurement corresponded to 500 s integral sampling duration.

ATR-FTIR was utilized to examine the particle purity. Therefore, a Vertex® 70 spectroscope was used. The absorbence was measured in a wavelength-range of 370–4500 cm^{-1} with 4 cm^{-1} resolution, by means of a HeNe laser at 633 nm. All samples were measured using a platinum holder in ATR technique.

XRD was carried out to derive information about the particle polydispersity and the phase composition. Measurements were carried out on a Bruker D8 Advance instrument in Bragg-Brentano mode with Cu K-α radiation (1.54 Å; 40 kV and 40 mA). A silicon single crystal with a crystallographic (911) plane was used as a sample holder to minimize scattering. A few milligrams of sample were applied over a large area on the crystal with sufficient layer thickness (>1 μm) to exclude further interferences of the holder. For better homogenization, the dried powder samples were redispersed in EtOH. Each sample was investigated in the range from 5 to 90° 2Θ with a step size of 0.01° Θ and a counting time of 0.6 s at each step. Rietveld refinement using the program package TOPAS 4.2 from Bruker was performed to determine the average crystallite sizes ($d_{cryst,XRD}$), relative weights (wt%), and lattice parameters. $d_{cyst,XRD}$ was calculated using the Debye-Scherrer relation, Eq. (1) [63]. With K=0.89 (assuming spherical particles), λ the wavelength of the X-ray radiation, *FWHM* the full width at half maximum for a diffraction peak, and Θ the diffraction angle. For each Rietveld refinement, the instrumental correction was determined using a standard powder LaB_6 sample obtained by NIST as a standard reference (SRM 660b; $a(LaB_6)$ = 4.15689 Å).

$$d_{cryst,XRD} = \frac{K \cdot \lambda}{FWHM \cdot cos\Theta} \tag{1}$$

BET N_2 physisorption [64] was used to derive information about specific powder surfaces and corresponding average primary particle sizes. The specific surface area (S_A) was determined by using a Quantachrome Autosorb 6 at −196 °C after a vacuum sample degassing at 120 °C over night. The calculation was performed with five points in the relative pressure region between 0.1–0.3. The average size of primary particles was calculated ($d_{PP,BET}$) by relating the cumulative surface of all particles, $\sum_i S_i$, to their cumulative mass, $\sum_i M_i$. By assuming that all primary particles are of identical spherical form, and size, $d_{PP,BET}$ is given by Eq. (2). With S_{PP} and V_{PP} as surface and volume of each primary particle, N the total number of primary particles, and ρ as material density. Due to this definition, $d_{PP,BET}$ represents the surface equivalent, mass-weighted average primary particle diameter.

$$S_A = \frac{\sum_i S_i}{\sum_i M_i} = \frac{\sum_i S_i}{\rho \sum_i V_i} \approx \frac{N \cdot S_{PP}}{\rho \cdot N \cdot V_{PP}} = \frac{6}{\rho \cdot d_{PP,BET}} \tag{2}$$

2.4. Determining local particle size distributions

2.4.1. Quenching experiments

While synthesizing particles by SS2, aerosol samples were extracted along the centerline above the visible flame tip (~7 cm) using a HIAT probe, and subsequently characterized via SMPS. This approach was followed to determine local particle size distributions of aggregates/agglomerates. The HIAT probe was necessary to dilute the aerosol sample sufficiently. To verify whether extracted samples were sufficiently diluted or not, so-called quenching experiments were carried out. Therefore, at each *HAB* (7, 7.5, 8, 9, 10, 12.5, and 15 cm) the *DR* was increased stepwise and SMPS scans were conducted. In order to visualize the effect of performing quenching experiments already at this point, Fig. 3 shows the qualitative evolution of the mean particle diameter, $d_{m,em}$, as function of *DR* (re-illustrated from [37]). As indicated in **(a)**, $d_{m,em}$ approaches degressively a steady-state value (representing the

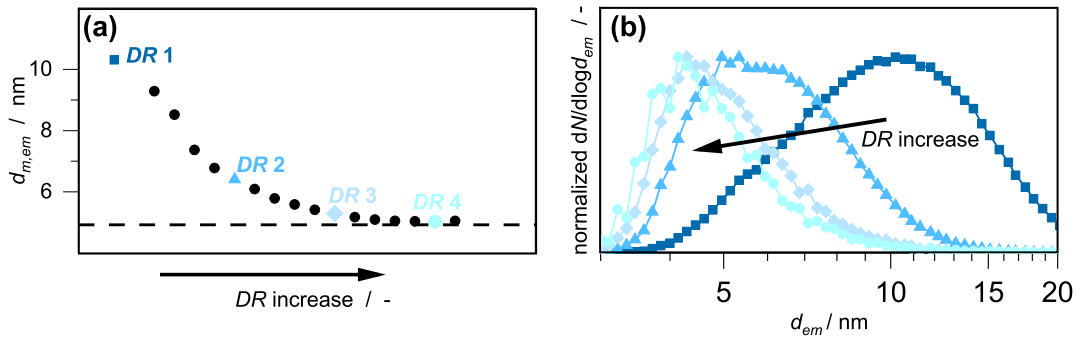

Fig. 3. Impact of changing *DR* in quenching experiments on SMPS measurements (qualitatively). With **(a)**: evolution of $d_{m,em}$ as function of *DR*, and **(b)**: shift/bias of size distributions at different *DR*.

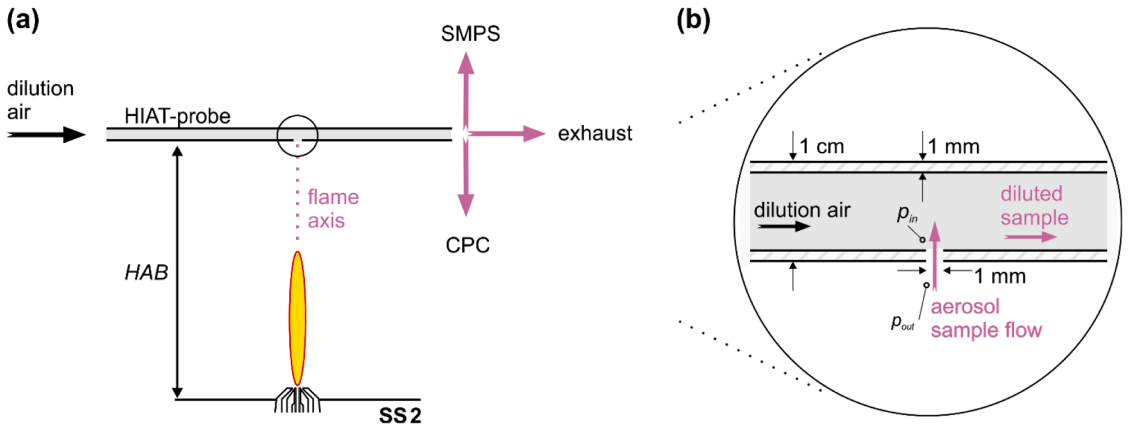

Fig. 4. Schematic sketch of the HIAT probe setup used. With **(a):** HIAT position illustration incl. SS2 burner, and **(b):** magnification of the sampling orifice. Note, arbitrary scales.

actual sample value). All values at lower *DR* are affected by agglomeration, yielding excessively high particle sizes. As shown in **(b),** this phenomenom is related to shifted particle size distributions.

2.4.2. *HIAT-SMPS configuration*

As shown in Fig. 4 **(a)**, a stainless steel tube was used as HIAT probe with dimensions of d_a=10 mm and $s = 1$ mm, and dried, particle-free air was introduced as dilution gas. Admittedly, for some material systems it may be useful to use inert gases such as nitrogen or argon to prevent oxidation. However, since maghemite was synthesized (see powder analytics later), using more expensive inert gases was obsolete. A cylindrical drilling of 1 mm diameter was used as orifice, employed in upstream orientation (hole points towards the flame). Hence, the *HAB* value corresponds to the distance orifice-burner. Note, lower drilling widths have been established widely for laminar diffusion flames with gas supply (especially 300 µm is the most common) [65–71]. In our approach, however, we found such small diameter tend to block, which is why we used 1 mm. Comparable, and even larger values (1–4 mm) were used by Goudeli et al. [51] and Gröhn et al. [52] in zirconia SFS-experiments. Each diluted sample was divided into three streams. The first substream was fed into a SMPS to measure the particles electrical mobility size distribution. This way, three characteristic quantities were derived, namely the mean mobility equivalent diameter of each distribution ($d_{m,em}$), its geometrical width (σ_{gn}), and the total particle number concentration ($c_{N,SMPS}$). Due to the SMPS measurement principle, $d_{m,em}$ and σ_{gn} are number-weighted. The second substream was fed into a stand-alone condensation particle counter (CPC). Indeed, a CPC is theoretically not necessary for performing quenching experiments (solely SMPS-data is necessary for the data evaluation). However, the CPC provided instantaneous particle concentration values ($c_{N,CPC}$) each second, which facilitated the adjustment and manipulation of *DR* considerably.

According to the literature, the operating principle of HIAT probes is based on the fact that a pressure difference (Δp) exists between the inside (p_{in}) and the outside of the orifice (p_{out}). This principle is shown in Fig. 4 **(b)**. Thus, *DR* can be controlled by manipulating p_{in}. As shown in studies on gas-fed laminar diffusion flames, there are multiple technical approaches how p_{in} and/or *DR* can be influenced. Some possibilities are the use of blowers or the introduction of additional gas streams (secondary gas) in the periphery [70]. Additionally Carbone et al. [71] presented, *DR*-values can also be manipulated by chaning the orifice width. In our setup, we manipulated the *DR*-value by changing the tube-internal gas flow rate (V_{quen}) representing a compareable simple option from technical point of view. In this context, high values of V_{quen} correlated with high *DR*-values and *vice vesa*. In our quenching experiments, V_{quen} was adapted in the range 15–100 L_N min^{-1}, corresponding to *Re*-values of ~2 600–17 000 (assuming atmospheric gas conditions in the tube). Note, such turbulent flows are advantageous to ensure a sufficient mixing of sample and dilution gas. But as shown numerically by Mätzing et al. [72], even higher *Re*-values would be necessary to ensure perfectly mixed samples.

2.4.3. *CPC and SMPS specifications*

SMPS- and CPC-devices from TSI Inc. were utilized. Regarding the SMPS, a steady-state charge distribution was generated using a soft X-ray radiator (type 3088) and a differential mobility analyser (DMA) of type 3086 was used, operated at 25 L_N min^{-1} sheath air. By using this DMA, negative particles in the size range 1–30.5 nm were classified. The number concentration of each mono-mobile particle fraction was determined using a butanol-based CPC (type 3750). To ensure a high

counting efficiency at ultra-small particle sizes, a so-called nano-enhancer (type 3757) was implemented upstream the CPC. Similar to the CPC, the enhancer increases particle sizes by means of a condensation mechanism. However, di-ethylene glycol (DEG) is used there as fluid. The SMPS was operated at the highest resolution, and size distributions were divided into 189 size-bins. The scan time was set at 60 s, the sample flow rate at 2.5 L_N min^{-1}. For the stand-alone CPC (type 3775, butanol-based) a sample flow rate of 1.5 L_N min^{-1} was applied. Note, the samples particle number concentration was also traced by the CPC. And since the stand-alone CPC had a high cut-off size (4 nm) comparing to the SMPS system (1 nm cut-off), it yielded systematically lower number concentrations.

2.4.4. Relevance of knowning DR-values

Knowing *DR*-values offers the opportunity to determine *in situ* particle number concentrations. For this purpose, as described for the first time by Zhao et al. [70], the number concentration measured by SMPS must be corrected by the *DR*-value. In addition, the number concentration has to be corrected according to the temperature relations (the samples' gas volume contracts during its extraction). As shown by studies on laminar gas diffusion flames, it is common to calibrate HIAT-probes *ex situ* (determining the dependency of p_{in} and *DR* experimentally). As mentioned, the sample volume flow is affected according to the pressure difference Δp, but it is additionally dependent on the physical properties of the sample. For instance, Zhao et al. approximated the sample volume flow passing the orifice using a laminar pipe flow according to Hagen-Poiseuill's law [70] *(3)*. With s as the wall thickness, $d_{orifice}$ as the drilling diameter, η as the gas viscosity, and c the calibration factor:

$$DR = 3.4 \cdot V_{quen} \cdot \left(c \cdot \Delta p \cdot \frac{\pi \cdot d_{orifice}^4}{s \cdot \eta} \right)^{-1} \quad (3)$$

We also intended to obtain information about local particle concentrations. And hence, were also characterized our HIAT probes by *ex situ* calibration approaches. In our approaches, probes were placed in upstream orientation in a stream of a NaCl test aerosol, yielding progressive functions of *DR* with rising p_{in} (e.g., calibration curve in Fig. S2). As shown, *DR*-values were very sensitive to p_{in}. And especially at higher *DR,* we noticed up to tenfold *DR*-values by solely changing p_{in} by 10 Pa. The high sensitivity of p_{in} to *DR* is in our opinion a major challenge for the application of HIAT probes including their calibration functions for SFS processes. So in SFS, turbulent flow fields are present typically. Due to the high sensitivity of our *DR-values* to the tubes pressure conditions, we assumed *DR* will unavoidably be subject to strong temporal fluctuations *in situ*. Hence, we did not used calibration curves for calculating local *in situ* particle concentration values, and the term 'dilution ratio' is used qualitatively in this paper. We want to emphasize, due to the high velocities present in/above the visible flame, fluctuations of the static pressure might be very intense. Probably, even the sign of the pressure values may flip.

Nevertheless, we intend to determine average *DR* values by calibration approaches in future. Therefore, however, average pressure conditions along the flames centerline should be known. Furtheremore, it could be beneficial to use HIAT-probes whith less sensitivity to pressure fluctuations (Δp, p_{in}, p_{out}). This could be realized by technical adaptations, i.e., by reducing the orifice width combined with much higher differential pressures (lower pressures within the probe). However, such technical changes will be accompanied by other challenges. For instance, SMPS devices are not designed for strong vacuum, and low orifice diameters can block quickly in SFS at low *HAB*. We have observed blocking even with our 1 mm probe at <7 cm *HAB*. Anyway, some alternative sampling concepts should be employed systematically in the future. In this regard, *DR*-values derived from the theoretical calibration models could additionally be validated by quantifying gas species stemming from the flame reaction using mass spectroscopy [71].

2.4.5. Relevance of diffusion corrections

Particle depositions by diffusion lowers particle number concentrations and can bias measured particle size distributions accordingly. Hence, when extracting particles by intrusive sampling, one should take diffusion losses into account. By using the setup of this study, particles can depose within three locations, namely (a): inside the orifice, (b): inside the tube, and (c): inside the SMPS device. In our approach, losses in (c) were taken into account by the manufacturer's software routine (AIM 11). As shown later (Section 3.2.1), SMPS-internal losses were rather high (reducing number concentrations in the lower double-digit %-range). Losses in (a) and (b) were estimated by us via analytical calculations, and graphical illustrations incl. calculation details can be found in the supplement (Fig. S3). There, the terminologies '(a)' and '(b)' are used similar and loss functions are shown for exemplary particle sizes (2.5 nm, 5 nm, 10 nm). Briefly, losses in **(b)**, which are mainly depending on the quenching gas flow V_{quen} are moderate. For instance, by assuming 293.15 K as gas phase temperature in the tube, loss-values are at 12 %, 5 % and 2 % for those exemplary particle sizes. In contrast, losses in **(a)** can attain much higher values, especially at high *DR*. Note, *DR* is defined in Fig. S3 as the ratio of total volume flow ($V_{quen} + V_{sample}$) to the sample volume flow V_{sample}. Hence, a high *DR*-value implies a low sample flow rate (going ahead with high residence times and high losses). As illustrated in (a) at high DR (e.g., DR = 10^5) loss-values of 35 %, 16 %, and 7 % result (which are comparable to SMPS internal losses). Those brief calculations exemplarily present that diffusion losses in (a) and (b) can affect size distributions to certain extend. And hence, they should be considered in general. However, in this study data was solely corrected by SMPS internal losses, (c), and losses in (a) and (b) are excluded. We decided this way, to not implement speculative loss calculations (temperature conditions and *DR* values are not known with high certainty). Having in mind the presented HIAT-SMPS data was solely corrected by SMPS-internal losses, particle sizes should be overestimated slightly. In future approaches, HIAT internal losses could be considered. Therefore it is necessary to determine *DR,* as well as tube internal temperature conditions.

3. Results and discussion

3.1. SS1 vs. SS2 powder comparison

In the first part of our study, we compared powders made by SS1 and SS2 by Raman, BET, XRD, and ATR-FTIR in terms of the phase compositions, particle size, and purity. To achieve a dominant gas-to-particle conversion a precursor composition containing INN dissolved in EtOH+2-EHA was used.

3.1.1. Raman

Raman spectroscopy is a well-established method for phase identification, since the three main iron oxide phases (magnetite, hematite, maghemite) show unique peaks in the ~150-800 cm^{-1} regime [4,8,9,14–16,50] Thus, SS1 and SS2 powders were characterized in this range, and their spectra features were compared to references (Fig. 5). The spectra shown in **(a)** and **(c)** represents averaged data from measurements at three different positions. The corresponding standard deviations are illustrated as areas around the curves. In panel **(a)**both powder spectra are compared in 150–800 cm^{-1}. References for hematite, maghemite and magnetite according to Faria et al. [73] are show above in **(b)**. The experimental peak positions were compared with a certain bandwidth of references in our study (Table S2). Since the references published by de Faria et al. are in consensus to the literature [62,74–77], they can be considered as representative.

According to the literature (Table S2), hematite shows seven active phonons/maxima, namely at ~225–230 (A_{1g}), ~245–250 (E_g), ~290–295 (E_g), ~299–302 (E_g), ~407–414 (E_g), ~491–500 (A_{1g}), and 608–615 (E_g) cm^{-1}. The phonon at ~290–295 cm^{-1} is the most intense,

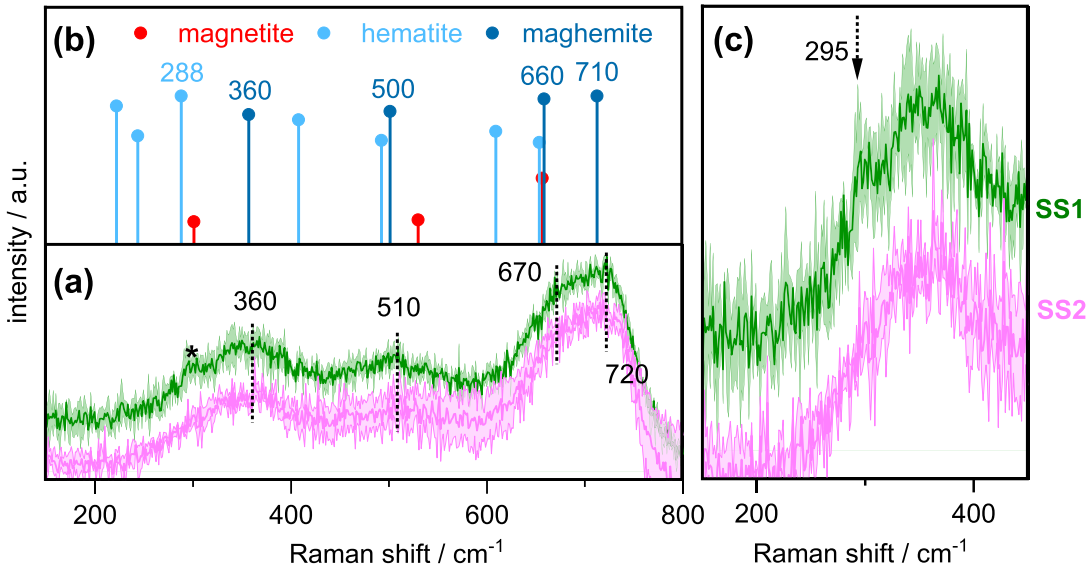

Fig. 5. Raman spectra of iron oxide samples made by SS1 and SS2 (processing 0.2 M INN in EtOH+2-EHA as precursor composition). Measurements were performed on powder samples derived by extracting the aerosol at 20 cm HAB (fume hood position). With **(a)**: experimental powder spectra, **(b)**: reference positions of Raman active vibrations of magnetite, maghemite, and hematite according to de Faria et al., and **(c)**: experimental spectra magnification.

followed by the ~225–230 cm^{-1} position. In addition, a longitudinal vibration at ~654–663 cm^{-1} can appear if impurities/crystal defects are present [74,78]. The peaks of hematite are usually very sharp. For maghemite, at least three vibrations appear which usually form quite broad maxima. They exist at the locations ~350–381 (T_{2g}), 486–512 (E_g), and 700–730 (A_{1g}) cm^{-1}. Some authors also presented shoulders/maxima at 665–670 cm^{-1}. A possible reason for this slight literature discrepancy is the fact maghemite can has considerable crystallographic differences. Magnetite also forms at least three broad vibrations. However, they are positioned at ~300–310 (T_{2g}), ~332–554 (E_g), and ~661–672 (A_{1g}) cm^{-1}. Latter one is the dominant vibration, and is usually sharply pronounced.

Considering the references, the experimental spectra revealed that dominantly maghemite was produced with both burner types. So, in each spectrum the global maximum was at 720 cm^{-1}, and two local maxima were found at 525 and 350 cm^{-1}. If hematite would be dominant, numerous sharp peaks should be pronounced with global maxima at ~290-295 cm^{-1}. In case magnetite would be present dominant, the three maxima should be at other positions. Interestingly, the averaged spectrum of the SS1 powder showed a weak intensity in the region around ~300 cm^{-1}. This region is highlighted by an asterisk in **(b),** and magnified in **(c)**. As illustrated in **(c)**, an additional maximum was found at ~295 cm^{-1} within the SS1 spectrum, which corresponds to the global maximum of hematite. Therefore, Raman indicated a hematite presence in the SS1 sample. In contrast, for SS2, no evidence of hematite was given. For both samples, the identification of the shoulder at 660 cm^{-1} was ambiguous. On the one hand it was described in the literature for maghemite. However, on the other hand, a feature at this position also indicates magnetite. For this reason, the SS1 sample was subsequently characterized by Mössbauer spectroscopy ruling out a relevant precence of Fe^{2+} (Fig. S4). Noteworthy, even Mössbauer measurements do not completely rule out the presence of minor magnetite traces (some few wt %).

3.1.2. BET

As shown in recent studies, iron oxide particles dominantly evolve by the gas-to-particle synthesis route using the precursor composition applied (INN in EtOH+2-EHA) [15,16,18,37]. This way, agglomerates and aggregates evolve consisting of spherical and hexagonal primary particles. And since primary particle sizes are mostly homogeneous in such samles, the average primary particle diameter ($d_{PP,BET}$) can be estimated using Eq. (2). Admittedly, the equation assumes all primary particles are monodisperse and spherical (which is a simplification). Nevertheless, Eq. (2) represents an established estimation method in literature. The values of S_A and $d_{PP,BET}$ are illustrated for SS1 and SS2 in Fig. 6. As visualized, SS2 yielded a 38 % higher S_A, and thus, a correspondingly smaller $d_{PP,BET}$. In particular, the value of $d_{PP,BET}$ for SS2 was 5.3 nm compared to 7.3 nm for SS1. The fact that SS2 produces smaller primary particles was evidenced by us in further experiments. For instance, we used 0.1 M INN instead of 0.2 M in the precursor solution, and the synthesized powders were characterized by BET as well. By reducing the precursor concentration this way, SS2 yielded S_A=248 m^2 g^{-1} with $d_{PP,BET}$=5.0 nm, while SS1 resulted in S_A=195 m^2 g^{-1} corresponding to $d_{PP,BET}$=6.3 nm. The subsequent powder measurements (XRD, ATR-FTIR) were performed on the sample derived from using 0.2 M INN.

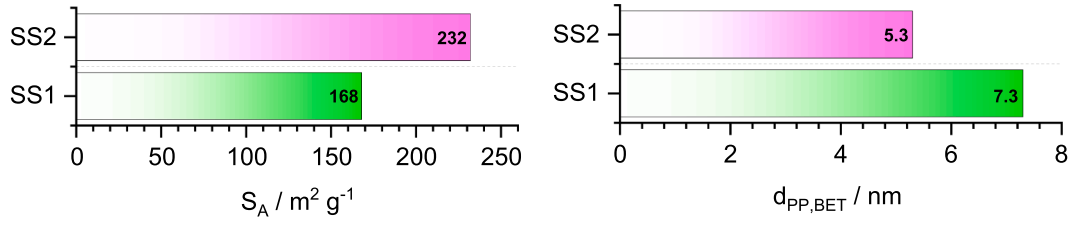

Fig. 6. BET measurement data of iron oxide samples made by SS1 and SS2 (processing 0.2 M INN in EtOH+2-EHA as precursor composition). Measurements were performed on powder samples derived by extracting the aerosol at 20 cm HAB (fume hood position). Left: S_A values. Right: $d_{PP,BET}$ values.

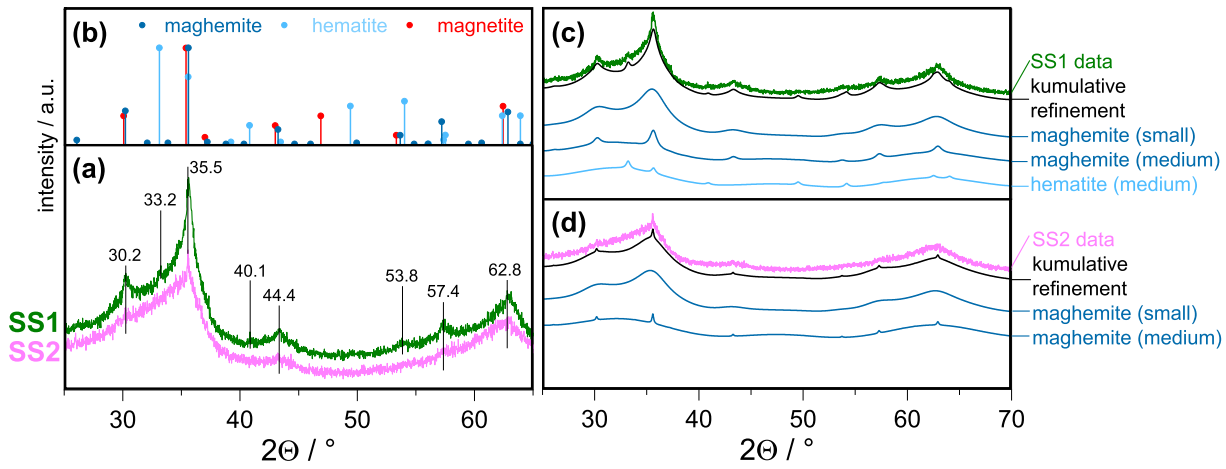

Fig. 7. XRD measurement data of iron oxide samples made by SS1 and SS2 (processing 0.2 M INN in EtOH+2-EHA as precursor composition). Measurements were performed on powder samples derived by extracting the aerosol at 20 cm HAB (fume hood position). With **(a)**: SS1 vs. SS2 diffraction pattern comparison (reflex positions indicated), **(b)**: PDF reference reflex positions, **(c)**: SS1 refinement data, **(d)**: SS2 refinement data.

3.1.3. XRD

XRD analyses including Rietveld refinements were performed to obtain quantitative information about crystallite sizes and phase compositions (Fig. 7). This way previous statements/assumptions made by Raman and BET were verified. Since a Bragg-Brentano optic was used (alignment procedure), XRD was not point-selective. This represented an important advantage of the XRD measurement, especially in terms of phase identification comparing to Raman. The experimental diffractograms of SS1 and SS2 powders are compared without refinement in **(a)**. Above, in panel **(b),** reference values for hematite ($R\bar{3}c$, PDF 33–0664), maghemite ($P4_332$, PDF 39–1346), and magnetite ($Fd\bar{3}m$, PDF 19–0629) are provided. Due to the Raman and Mössbauer measurements a presence of magnetite was neglected in the XRD analyses. Thus, the magnetite references are solely presented for completeness. Results of Rietveld refinements are illustrated for SS1 in **(c),** for SS2 in **(d)**.

XRD analysis revealed interesting similarities but also differences between both powders. As shown in **(a)**, samples had in common that they produced very amorphous diffractograms. There, both pattern show global maxima at 35.5°, and four other local maxima at 30.2, 44.4, 57.4, 62.8 °. The diffractions were considerably broad, which evidenced the presence of small particles <5 nm. The reference values in **(b)** revealed maghemite as corresponding phase. Therefore, small-sized maghemite <5 nm was indicated as dominant phase for both samples. Besides the commonality of a dominant, small-sized maghemite fraction, two major differences were found. On the one hand, as shown in panel **(a)**, additional weak diffractions were present at 33.2, 40.1, and 53.8 ° for SS1, indicating the presence of hematite. Since the diffraction at 33.2 ° was relatively sharp, hematite particles were identified as 'medium-sized' (double-digit nm-range). For SS2, in contrast, no evidences for hematite particles were found. On the other hand, both samples clearly revealed maghemite particles are present with certain polydispersity. To illustrate this phenomenom, the refinements of SS1 **(c)** and SS2 **(d)** have to be considered. There, the top curves represent the experimental XRD data, below refinement data is shown. As shown, solely including a small-sized maghemite fraction did not represent the shape of the diffractions at 35.5 ° correctly. At this position, the expermimental diffractions were much spikier towards the top. Consequently, it was necessary to consider a further (medium-sized) maghemite fraction.

The qualitative similarities and differences described above were quantified in the refinement, visualized in **(c)** and **(d)**. As mentioned, three fractions were identified in the SS1 sample (small-sized maghemite, medium-sized maghemite, medium-sized hematite), two for SS2 (small-sized maghemite, medium-sized maghemite). The fractions weight percentages (wt %) and average crystallite sizes ($d_{cryst,XRD}$) are compared in Table 3. Due to the highly amorphous behaviour, the refinement is subject to some uncertainty. Nevertheless, the comparison evidenced small-sized maghemite particles were present with higher content for SS2 (98 %), comparing to SS1 (86 %). The higher wt % of small-sized maghemite in the SS2 sample was essentially caused by the fact medium-sized maghemite particles were less prominent (2 % for SS2 vs. 11 % for SS1). In addition, SS1 produced an additional medium-sized hematite fraction (3 %) which was not noticeable for SS2. Qualitatively the XRD Refinement data agreed with the size tendencies of BET measurements, and with phase identifications made by Raman.

Table 3
Powder compositions of iron oxides manufactured by SS1 and SS2 (processing 0.2 INN in EtOH+2-EHA as precursor composition). Data was derived using XRD incl. Rietveld refinement.

	SS1	SS2
medium-sized hematite (R3c, PDF 33-0664)	**20 nm** **3 wt %** ($a \approx 5.03$ Å) ($c \approx 13.72$ Å)	*not considered*
medium-sized maghemite ($P4_332$, PDF 39-1346)	**10 nm** **11 wt %** ($a \approx 8.36$ Å)	**55 nm** **2 wt %** ($a \approx 8.34$ Å)
small-sized maghemite ($P4_332$, PDF 39-1346)	**~2-3 nm** **86 wt %** ($a \approx 8.36$ Å)	**~2-3 nm** **98 wt %** ($a \approx 8.36$ Å)

3.1.4. ATR-FTIR

SFS-generated particles can carry organic impurities on their surfaces (surface adsorbates). Hence, we also employed differences in the samples chemical purity using ATR-FTIR (Fig. 8). By using IR spectroscopy, information about bond types and functional groups were obtained from peaks in the IR spectrum (which represent IR-active molecular vibrations). In Fig. 8 each powder spectrum was normalized to its maximum in the lower wavelength range (<800 cm^{-1}). This range <800 cm^{-1} is magnified in **(b)**. As illutrated there, a global maximum was found at ~580 cm^{-1} for both powders which is characteristic for vacancy-disordered maghemite. This was demonstrated, for example, by Li et al. on SFS-made maghemite with $d_{cryst,XRD}$<8 nm [9]. In higher wavelength regions (see **(a)**), additional intense peaks were found at 2962, 2935, 2877, 2867, ~1645, ~1520, ~1420, and ~1300 cm^{-1}. A shoulder existed additionally at ~1460 cm^{-1}. In order to identify the peaks, we compared them to literature values, revealing the presence of

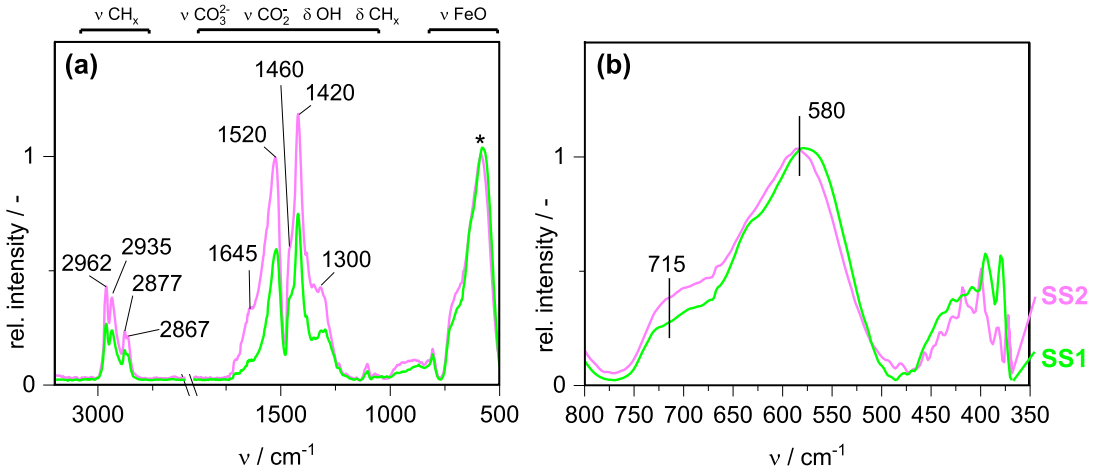

Fig. 8. ATR-FTIR measurement data of iron oxide samples made by SS1 and SS2 (processing 0.2 M INN in EtOH+2-EHA as precursor composition). Measurements were performed on powder samples derived by extracting the aerosol at 20 cm HAB (fume hood). With **(a)**: full spectra, and **(b)**: magnification of the FeO vibration regime.

organic species. Thus, the quartets at 2962, 2935, 2877, and 2867 cm^{-1} were caused by stretch vibrations of methyl and methylene groups [79,80], indicating aliphatic structures in both samples. Moreover, the strongly pronounced double peaks at 1420 and 1520 cm^{-1} indicated surface-bound carboxylates (R-CO_2^-) and carbonates (CO_3^{2-}) [11–13,55,79–82]. Those peaks corresponded to C-O stretch-vibrations. Hence, the aliphatic groups identified are probably associated in the carboxylates molecular rest, R. As shown in **(a)**, organic vibrations were more intense for SS2, indicating higher relative amounts of organic impurities. We explain this phenomenom by the fact impurities were attached on particle surfaces. Hence, SS2 powders may carry a higher relative amount of impurities, causing higher intensities. Based on the ATR-FTIR measurements, we assumed the surface-associated aliphatic structures may yield hydrophobic particle surfaces. We subsequently attempted to disperse both powder samples in water - without success.

In this context we mention the ATR-FTIR measurements influenced the choice of the appropriate SMPS system for the subsequent HIAT-SMPS experiments. In fact, at the beginning of our study, we had two different SMPS systems available: One SMPS system which had been using a water-based CPC and a second system using a butanol CPC including DEG enhancer. Since we assumed that hydrophobic particle surfaces indicated by ATR-FTIR may influence the counting efficiencies of water CPCs, we deliberately selected the latter SMPS configuration (see method section). Noteworthy, also DEG- and butanol-CPCs show certain sensitivity to the particle surface/polarity [83,84]. However, this takes place dominantly at the lower detection limit. Considering the comparable large particle sizes measured during quenching experiments, and due to usage of both, a butanol-CPC and a DEG-CPC in series, sufficient high counting efficiencies should be obtained. It would be very interesting to characterize extracted samples also with water-based SMPS systems in future to quantify our expected bias.

3.2. Aggregate/agglomerate size distributions for SS2

In the second part of our study, quenching experiments were conducted while generating iron oxides using SS2. Thus, particle size distributions were measured along the flame centerline (7–15 cm HAB) using the HIAT-SMPS coupling. In this approach 0.2 M INN dissolved in EtOH+2-EHA was used as precursor composition.

3.2.1. Quenching experiments and HIAT-SMPS data

For interpreting the quenching experiments, SMPS data has to be considered as shown in Fig. 9. There, $d_{m,em}$ and σ_{gn} are depicted as function of $c_{N,SMPS}$. According to the sampling principle, higher $c_{N,SMPS}$-values reflect low *DR*, and *vice versa*. To illustrate the influence of SMPS-internal diffusion losses, data without diffusion correction (open symbols) and with diffusion correction (filled symbols) are shown. As can be seen, the SMPS-internal loss was comparatively high compared to the other diffusion losses (see Section 2.4.5). Therefore, it is highly recommended to take SMPS-internal losses into account. Complete data sets can be found on SpraySyn.org. There, V_{quen}-values, and further SMPS data (e.g., all distribution functions) are provided. There, also values for $c_{N,CPC}$ are available, which have been considerable lower than $c_{N,SMPS}$ (due to the CPCs limited counting efficiency).

In order to interpret functions of $d_{m,em}$ and σ_{gn}, it is necessary to refer to the basic knowledge about the self-preserving nature of aerosols, which is considered to be very well studied so far [85–90]. In general, particles which interact in aerosols by agglomeration and sintering tend to develop characteristic values for their distribution widths, σ_{gn}. In this regard, steady-state σ_{gn}-values depend on the motion regime (continuum/transition/free molecular) and on the dominance of agglomeration or sintering. The motion regime of the particles within the HIAT probe was determined by estimating the Knudsen number, *Kn*. And by taking into account the experimental $d_{m,em}$ values and assuming atmospheric conditions in the tube, *Kn* values corresponding to the free-molecular regime were determined (e.g., *Kn*=8.87 for 15 nm, *Kn*=26.61 for 5 nm). In this motion regime, sintering dominance yields spherical particles with rather narrow distributions, σ_{gn}=1.46 [87,90]. In contrast, at negligible sintering activity (solely agglomeration), broader distributions form with σ_{gn}=2.03, while particles become fractal [87,90]. As shown at each *HAB* position, the decrease of *DR* (higher $c_{N,SMPS}$), yielded increased $d_{m,em}$- and σ_{gn}-values. For example, at *HAB*=9 cm, the value of $d_{m,em}$ increased from 7 to 12 nm, while σ_{gn} increased from 1.45 to 1.55 simultaneously. Considering the reference values mentioned above, the progressive evolution of $d_{m,em}$ and σ_{gn} with decreasing V_{quen} indicated particles are present with narrow distributions *in situ*. However, once samples were extracted, they agglomerated along the measurement section yielding higher σ_{gn} and $d_{m,em}$. It can be seen, the manipulation of V_{quen} had a considerable influence on $d_{m,em}$ at all *HAB*. For example, at 7 cm, the asymptotically value for $d_{m,em}$ appears to be at ~7 nm. In contrast, at insufficient dilution, $d_{m,em}$ increased up to ~12 nm. On higher *HAB*, the influence of dilution was lower (~11 nm vs. ~15 nm at 15 cm *HAB*).

Interestingly, at low *HAB*s, we found that σ_{gn} also increased for very low $c_{N,SMPS}$. Hence, σ_{gn} graphs yielded concave profiles at 7, 7.5, and 8 cm. In fact, this behaviour was contradictory to our expectations at first glance, as we assumed that high *DR* should always result in a decrease of

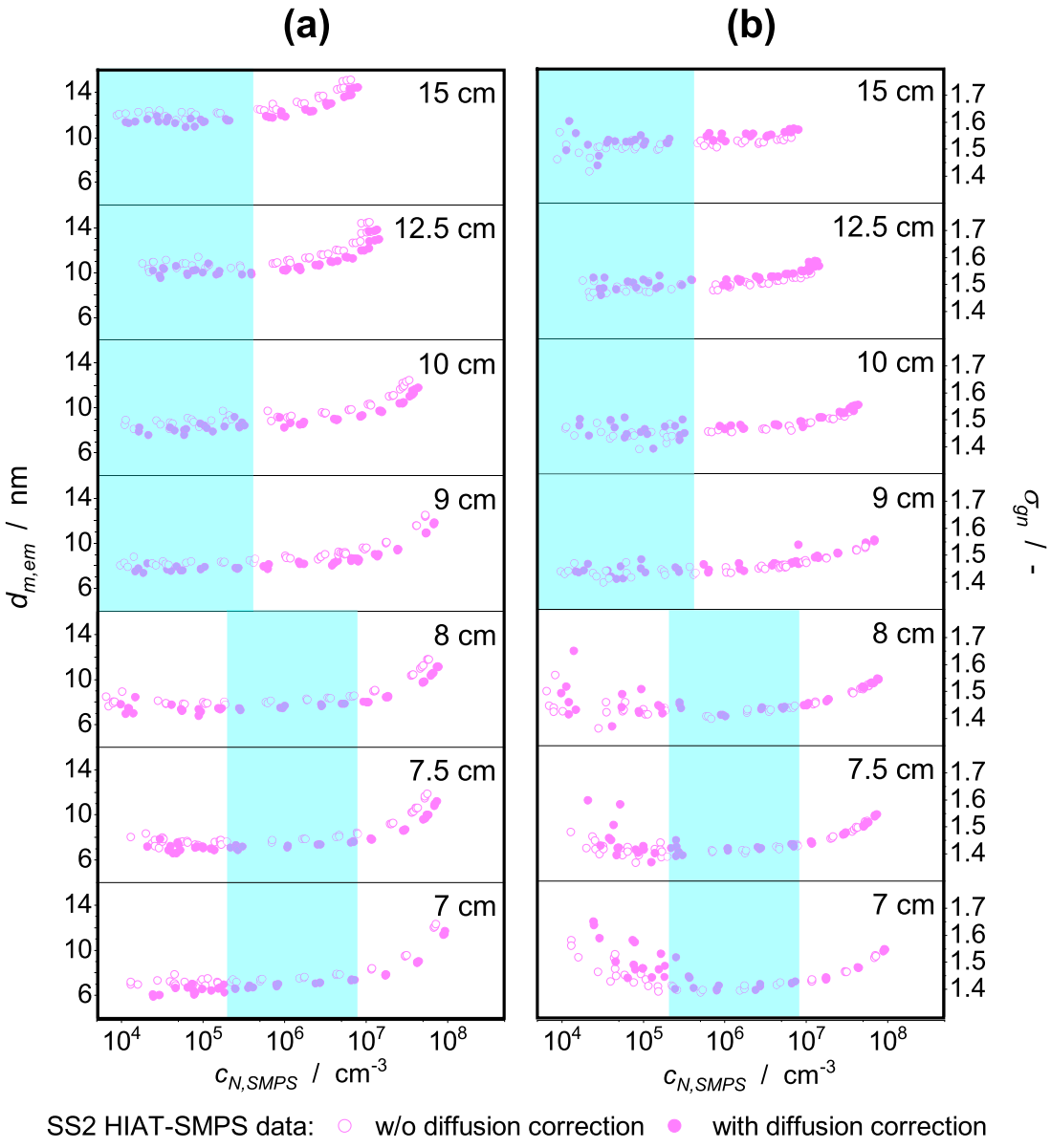

Fig. 9. Particle data derived by HIAT-SMPS measurements at various dilution ratio and various *HAB*. In those experiments iron oxide particles were fabricated using SS2 as burner and 0.2 M INN in EtOH+2-EHA as precursor composition. Each point represents data derived from one particle size distribution (one SMPS scan). With **(a)**: $d_{m,em}$ (the mean number-weighted electrical mobility equivalent diameter), and **(b)**: σ_{gn} (the number weighted geometric distribution width). Both, $d_{m,em}$ and σ_{gn}, are presented as function of $c_{N,SMPS}$. In this regard, low $c_{N,SMPS}$ values represent low dilution ratios and *vice versa*.

$d_{m,em}$ and σ_{gn}. To identify the reason for this phenomenon we qualitatively compared several particle size distributions. In this regard, Fig. 10 compares three distributions at 7 cm and 15 cm *HAB*, respectively. Reading from left to right, distributions were measured at increasing $c_{N,SMPS}$: left at low (~2 × 10^4 # ml^{-1}), central at medium (~2 × 10^5 # ml^{-1}), and right at high $c_{N,SMPS}$ (~10^7 # ml^{-1}). As explained above, distributions with high concentrations were subject to a bias by agglomeration. For this reason, right distributions were visibly shifted along the x-axis compared to the middle distributions (accompanied with higher σ_{gn} -values). Taking a look at the 7 cm *HAB* distribution measured at low $c_{N,SMPS}$, strong contributions in the <~5 nm region were apparent. This region is magnified in Fig. 10. There it can be seen, the size distribution function increased towards smaller d_{em}, which caused the σ_{gn} increase. This interesting phenomenon can be explained by two approaches. First, a second mode in the size distribution is indicated. As shown by soot studies [65,66,91], the development of bimodal particle size distributions is not uncommon for flame aerosols, and we think that the emergence of bimodalities cannot be ruled out for this SFS setup as well. Those bimodalities can evolve due to charging effects. And it is also known the coagulation coefficient can be affected by the particle size additionally (often below 5 nm) which can cause bimodal distributions [92]. Since such bimodal size distributions would result in even higher aggregation kinetics, they could be detected for very low concentrations only. Secondly, according to the manufacturer's information, signals <5 nm can represent measurement artifacts, in case the automatic data processing routine (conducted by AIM 11) overcompensates SMPS-corrections. Those overcompensations can take place if very low number concentrations are present in SMPS measurements [93]. The question why this systematic bias is pronounced only on the lower *HAB* (7, 7.5, and 8 cm) can be justified by the fact much smaller particles were present at lower *HAB*. So as the charge probability is lower for small particles [94], less particles have been physically present in the SMPS scan at lower *HAB*, even though, final (re-calculated) $c_{N,SMPS}$-values are similar. This phenomenom is also caused by the

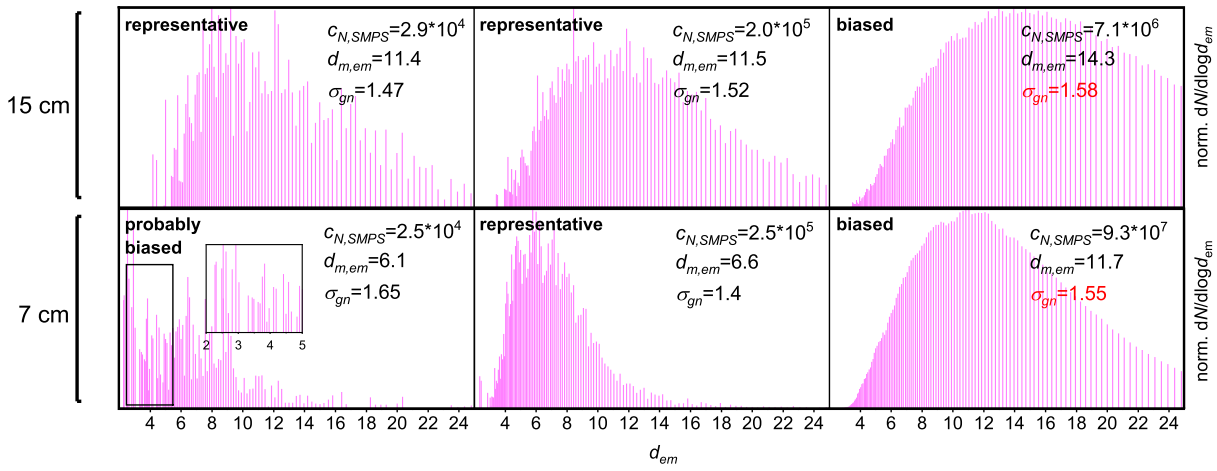

Fig. 10. Comparison of particle size distributions at 7 cm (bottom row) and 15 cm *HAB* (top row). In each row measured $c_{N,SMPS}$ increases from left, to middle, to right. Note, each size distribution was normalized to its maximum. Also note, concentration units are in # cm^{-3}, particle sizes are in nm.

limited counting efficiency of the CPC/Enhancer combination [95,96]. Thus, at lower *HAB*s (lower particle sizes) less particles were actually physically comparing to measurements at higher *HAB*s (larger particle sizes), even though re-calculated number concentrations are equal.

3.2.2. *Definition of reliable $c_{N,SMPS}$-regimes and data averaging*

Considering the above mentioned issues, we defined areas within our dataset, where SMPS data appeared reliable (highlighted by blue boxes in Fig. 9). Above 8 cm, samples were considered representative in the case $c_{N,\ SMPS} < 4 \times 10^5$ cm^{-3}. At ≤8 cm, we had to make a compromise. In those cases, measurements appeared reliable in the range 2×10^5 $cm^{-3} < c_{N,\ SMPS} < 8 \times 10^6$ cm^{-3}. Within those ranges, we calculated arithmetic means ($\overline{d_{m,em}}$ and $\overline{\sigma_{gn}}$) and corresponding relative sample standard deviations (s^2) for each *HAB* (Table 4). By evaluating the SMPS data this way, the quenching experiments reliability was qualified quantitatively. By averaging N^*=12 up to 18 measurements, s^2 was between 2.2 and 4.7 % in terms of $d_{m,em}$, while s^2 was between 1.1 and 2.2 % for σ_{gn}. Hence, a high reproducibility of SMPS measurements was indicated within defined $c_{n,\ SMPS}$-regions. In Table 4, two further analytical parameter are presented for each *HAB*, namely $d_{m,em,bias}$ and $\sigma_{ng,bias}$. They were calculated by relating the highest measured $d_{m,em}$ and σ_{gn}-value at each *HAB*, to its reliable average ($\overline{d_{m,em}}$ or $\overline{\sigma_{gn}}$). This way we quantified the maximal bias measured. The highest bias of $d_{m,em}$ ($d_{m,em,bias}$) was obtained at *HAB* 7 cm (~68 %) and decreased with rising *HAB* (e.g., ~26 % at 15 cm). This way it was quantitatively evidenced quenching experiments are even more important at low *HAB*. Note, the value of 68 % represents solely the highest bias value by reflecting our dataset and even higher bias values could go ahead at lower *DR*. $\sigma_{gn,bias}$ was also highest at lowest *HAB* (~9 %).

3.2.3. *Evolution of $\overline{d_{m,em}}$ and $\overline{\sigma_{gn}}$ along the centerline*

As previously shown by studies [51,52,97], the functional dependency of the mobility diameter along the centerline is sensitive to the dominance of particle formation mechanisms. Hence, the graphical visualization of $\overline{d_{m,em}}$ and $\overline{\sigma_{gn}}$ can yield some information about the dominances in synthesis mechanisms. For example, Gröhn et al. studied the formation of primary particle and aggregate sizes of ZrO_2 in SFS via intrusive particle extraction techniques (HIAT probing and thermophoretic sampling). In their approach, the evolution of the primary particle size was mostly complete at the flame tip (~10 cm with T=~1500 K in their study), which is why the evolution of mobility diameter above the flame tip >10 cm subsequently increased nearly linearly [52]. Similar trends were shown by numerical studies. For instance, Tsantilis and Pratsinis, computed the evolution of silica primary particle sizes and aggregates/agglomerate sizes by agglomeration and sintering interaction via population balances. As shown in their study for different temperature profiles, sinter dominance should

Table 4
Quantitative evaluation of the reliability of measured SMPS particle data. Values of $d_{m,em}$ and σ_{gn} values were averaged within reliable $c_{n,SMPS}$-ranges revealing $\overline{d_{m,em}}$, $\overline{\sigma_{gn}}$, and corresponding standard derivations (s^2). Additionally, at each *HAB*, the highest relative bias was calculated ($d_{m,em,bias}$ and $\sigma_{gn,bias}$). Those relative bias values were calculated by relating the most biased data point to the average $\overline{d_{m,em}}$ or $\overline{\sigma_{gn}}$.

considered data points for averaging			results from data averaging within the reliable $c_{N,SMPS}$ range				relating the most biased data-point (=highest value) to the reliable arithmetic mean	
			$d_{m,em}$		σ_{gn}			
HAB– height above burner / cm	$c_{N,SMPS}$ – range of reliable data / #/mL	N^* – number of included measurements / -	$\overline{d_{m,em}}$ – sample arithmetic mean / nm	s^2- relative sample standard deviation /%	$\overline{\sigma_{gn}}$ – sample arithmetic mean / -	s^2- relative sample standard deviation /%	$d_{m,em,bias}$ –maximum $d_{m,em}$ bias in this study /%	$\sigma_{gn,bias}$ –maximum σ_{gn} bias in this study /%
15	$5x10^3$ – $4x10^5$	18	11.4	2.2	1.52	2.2	26.2	3.4
12.5	"	18	10.0	3.2	1.5	1.3	37.0	5.6
10	"	18	8.2	4.7	1.46	2.1	43.5	6.3
9	"	15	7.7	2.7	1.44	1.3	53.0	7.9
8	$2x10^5$ – $8x10^6$	12	7.6	2.6	1.43	1.1	46.1	7.8
7.5	"	15	7.3	3.1	1.42	1.1	53.9	8.8
7	"	14	6.9	4.0	1.42	2.2	67.7	8.7

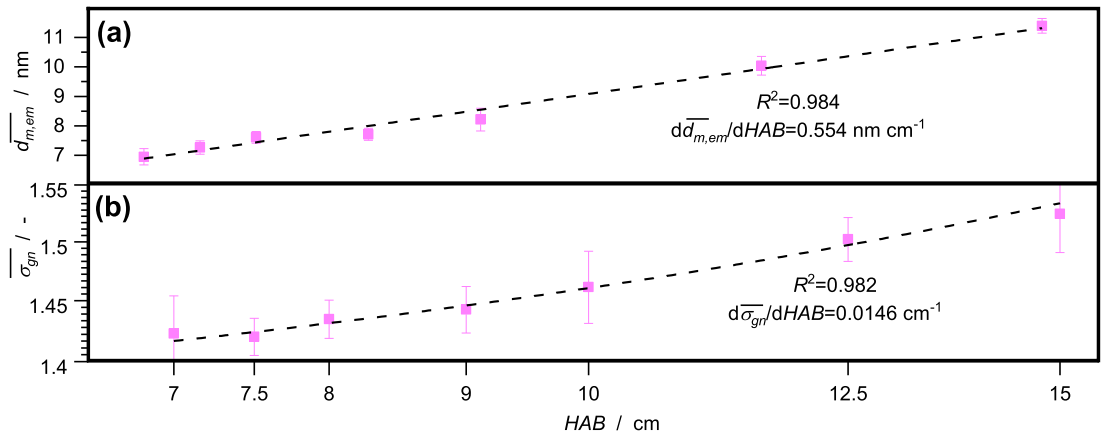

Fig. 11. Evolution of number-weighted, average particle structure properties along the centerline using SS2 for iron oxide fabrication (using 0.2 M INN in EtOH+2-EHA as precursor composition). With (a): evolution of $\overline{d_{m,em}}$, and (b): evolution of $\overline{\sigma_{gn}}$. Note, the error bars depicted represent the experimental standard deviation shown in Table 4.

manifest in extremely strong curvatures in the evolution of the average particle mobility size [97]. According to the literature, we have also illustrated $\overline{d_{m,em}}$ and $\overline{\sigma_{gn}}$ as a function of *HAB* and approximated the profiles by linear regression (Fig. 11). It can be seen that $\overline{d_{m,em}}$ growed apparently linearly with a good correlation in our case, indicating that the growth of the primary particles via agglomeration and sintering was

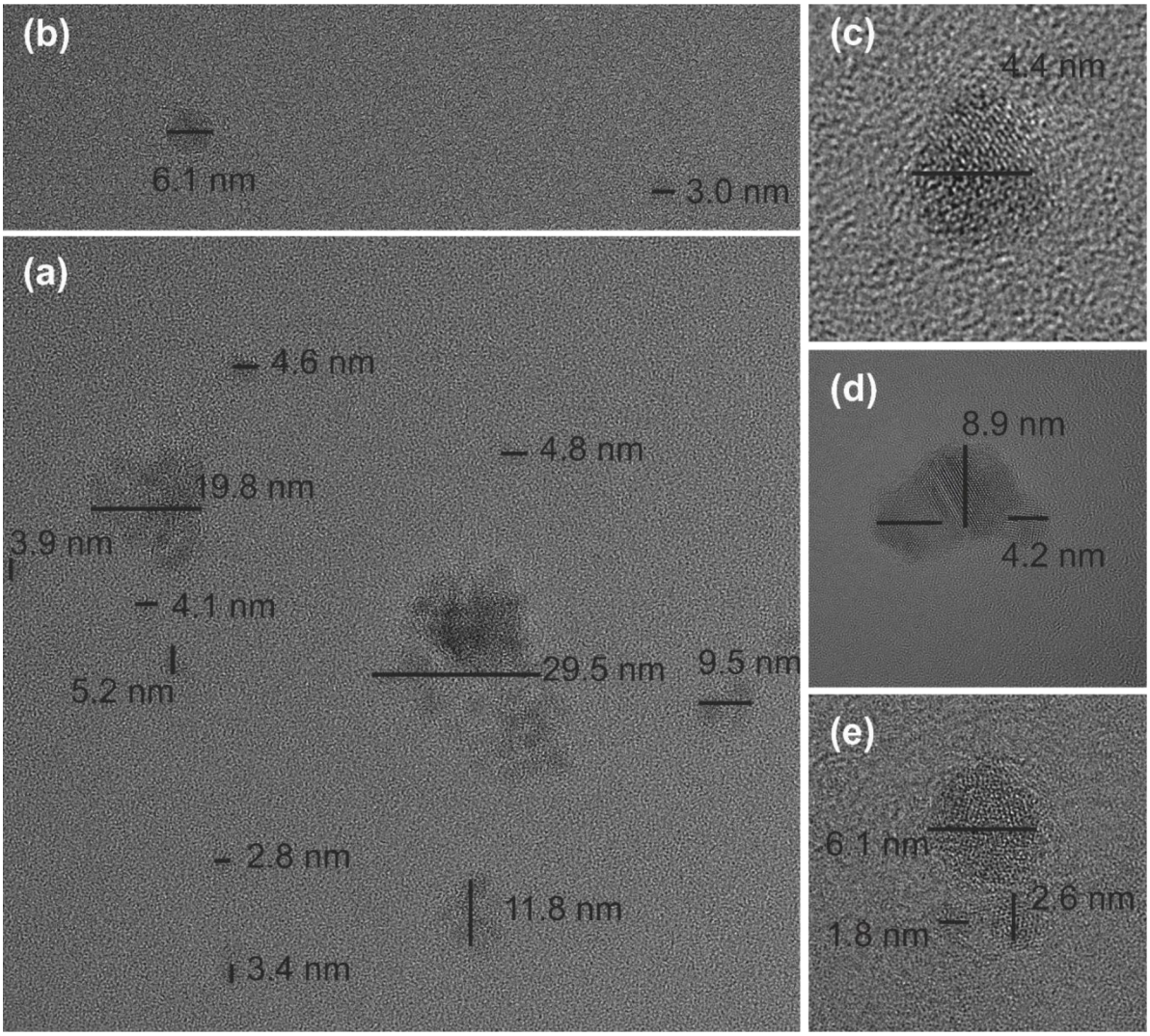

Fig. 12. Exemplary TEM illustrations showing iron oxide particles present at 7 cm *HAB* using SS2 as burner and 0.2 M INN in EtOH+2-EHA as precursor composition. Particles were extracted using a tailored thermophoretic sampler system and were subsequently examined by TEM (TS-TEM).

mostely completed in the *HAB* regime considered. Simultaneously to $\overline{d_{m,em}}$, also $\overline{\sigma_{gn}}$ growed linearly. The explanation for the growth of $\overline{\sigma_{gn}}$ has already been explained in the previous section and can also be used here. Thus, particle agglomeration under negligible sintering in the free molecular motion regime causes $\overline{\sigma_{gn}}$ to increase.

3.2.4. Particle morphology conclusions

By comparing the results of the powder analysis with the values of the SMPS measurements, one can derive an interesting information: the values of the final primary particles (as quantified by means of $d_{PP,BET}$ and $d_{cryst,XRD}$) were solely *slightly* smaller compared to SMPS sizes ($\overline{d_{m,em}}$). For instance, the final $d_{PP,BET}$ value was at 5.3 nm, while $\overline{d_{m,em}}$ increased *in situ* from ~7–11 nm. The fact SMPS-based agglomerates/aggregates sizes were close to the values of $d_{PP,BET}$ and $d_{cryst,XRD}$ suggested that most particles in the aerosol must have quite compact structures. To support this theory, we extracted samples at 7 cm *HAB* via thermophoretic sampling [98], and examined them using transmission electron microscopy imaging (TS-TEM). A suitable sampler has been developed in our laboratory, and has been extensively tested for such an extraction [37]. To prevent particles from overlapping on the TEM grid, the grid exposure time was limited to 2 ms. Additionally, the grid was protected physically on its way to the sampling position to avoid 'way sampling'. Exemplary TEM illustrations are shown in Fig. 12.

As shown in **(a)** under moderate magnification, particles were spread statistically on the grid with sufficient distance to each other. Consequently, particle structures did not overlap, and individual particle structures were recognized. In **(a)**, all (apparently) individual single particle structures were measured in size in respect to one spatial direction. As shown, most particles were in the <10 nm range. This fact was true for most areas of the grid. The image in **(a)** was chosen to show that also some *larger* agglomerates/aggregates were found. As illustrated there, two larger aggregates/agglomerates of ~20 and ~30 nm can be found in the centre. But even though such larger particles were found, they have been present with considerable lower number concentrations from subjective point of view. Most abundant particle structures are exemplarily shown in panels **(b)** to **(e)**. As can be seen in **(b)**, completely spherical, unaggregated single particles were found. Panel **(c)** shows such a particle in high resulution (HRTEM). There, individual crystal planes can be recognized, indicating a high particle crystallinity. In **(d)** and **(e)** some aggregate structures are shown. Interestingly, they solely included a few primary particles. For example, the particles shown in **(d)** and **(e)** consist of three (visible) primary particles. In summary, the TS-TEM analysis showed a dominant presence of single particles and non-fractal, compact particle aggregates/agglomerates. And the majority of structures were in the size-range indicated by HIAT-SMPS measurements at 7 cm HAB (already shown in Fig. 10). Larger particles were found, but their number concentrations were considerably low. Hence, the qualitative TS-TEM results confirmed the SMPS size distributions and the conclusions drawn in the respective section.

4. Conclusion

In the first part of our study iron oxide nanoparticles were fabricated by operating two different burner geometries (SS1 and SS2), at identical operating conditions. Therefore, a precursor composition known from literature was utilized. The comparison of particle properties was performed by Raman, XRD, BET and ATR-FTIR. As shown by Raman, both burner types yielded dominant maghemite particles. Interestingly, XRD revealed a certain polydispersity of this phase, as a small-sized fraction coexisted aside of a medium-sized fraction. This medium-sized fraction was less prominent within the SS2 sample. Additionally, Raman and XRD revealed a medium-sized hematite fraction for SS1, which was not apparent for SS2. Concluding the phase composition analysis, SS2 yieled a more homogeneous outcome of small-sized maghemite comparing to SS1. It is assumed the more homogeneous flame of SS2 may caused this increase in powder homogenity, and these effects should be subject of further investigations. BET and XRD additionally revealed SS2 tends to produce considerable smaller primary particle diameters compared to SS1. Hence, SS2 powders attained much higher specific surface areas. The powder purities were examined by ATR-FTIR, revealing a presence of aliphatic carboxylates and carbonates. The spectra comparison revealed more pronounced organic vibrations for SS2. This can be explained by the higher specific surface of SS2 powders, as those impurities are usually attached on particle surfaces. The presence of those species explains the powders strong hydrophobicity. In future it might be interesting to quantify and compare the purity of both powders by further techniques.

In the second part of this paper, we determined aggregate/agglomerate size distributions of iron oxides manufactured by SS2. Therefore, aersol samples were extracted along the centerline above the visible flame tip (>=7 cm) using a HIAT probe. The probe dilution ratio was manipulated in quenching experiments and extracted samples were characterized by SMPS. We reported the derived SMPS data in detail, and we presented challenges one has to face for the application of HIAT probes in SFS. It was demonstrated, that performing quenching experiments is absolutely necessary to suppress considerable agglomeration, and to consequently ensure a reliable data outcome. In future it would be interesting to repeat the HIAT-SMPS measurements using a water-based SMPS instead of the butanol-DEG system. We assume a certain experimental bias should be derived due to the strong hydrophobic particle surface when using water SMPS systems. The quantitative evaluation of quenching experiments revealed an almost linear increase of agglomerate sizes and distribution widths along the centreline, indicating that primary particle growth by agglomeration and sintering has already been completed at lower heights <7 cm. Interestingly, the mean agglomerate/aggregate sizes as determined via HIAT-SMPS were solely slightly larger than primary particle sizes previously measured by XRD and BET. This finding indicated particles of compact structures. As shown by TS-TEM the particle ensemble close to the flame tip (7 cm) was dominated by non-agglomerated, spherical particles and weakly aggregated structures <10 nm. Corresponding aggregates/agglomerates consisted in most cases solely of a few primary particles, and were not fractal in consequence. By TS-TEM, also larger aggregates/agglomerates were be found. However they were present with much lower number concentrations.

CRediT authorship contribution statement

Ricardo Tischendorf: Conceptualization, Data curation, Formal analysis, Investigation, Methodology, Validation, Visualization, Writing – original draft, Writing – review & editing. **Orlando Massopo:** Investigation, Methodology. **Oleg Prymak:** Data curation, Investigation, Methodology, Software. **Sophie Dupont:** Conceptualization. **Fabian Fröde:** Conceptualization. **Heinz Pitsch:** Project administration, Supervision. **Reinhold Kneer:** Project administration, Supervision. **Hans-Joachim Schmid:** Conceptualization, Project administration, Supervision.

Declaration of Competing Interest

The authors declare that they have no known competing financial interests or personal relationships that could have appeared to influence the work reported in this paper.

Data availability

The data shown is available on an open access data-base (SpraySyn.org), and the powder samples are accessable on request.

Acknowledgements

We kindly thank the DFG (German Research Foundation) for funding (Project Number 375857587 including SCHM 1429/13-1, KN 764/20-1, Pl 368/19-1). We also thank TSI Inc. for providing a 1-nm SMPS setup for performing SMPS measurements. The authors also thank Dr. Carsten Kykal for suggestive ideas and very valuable professional discussions during data interpretation, and Sven Klüsener for his support during performing experiments.

Supplementary materials

Supplementary material associated with this article can be found, in the online version, at doi:10.1016/j.jaecs.2023.100235.

References

[1] Strobel R, Pratsinis SE. Flame aerosol synthesis of smart nanostructured materials. J Mater Chem 2007;17:4743.
[2] Li S, Ren Y, Biswas P, Tse SD. Flame aerosol synthesis of nanostructured materials and functional devices: processing, modeling, and diagnostics. Prog Energy Combust Sci 2016;55:1–59.
[3] Teoh WY, Amal R, Mädler L. Flame spray pyrolysis: an enabling technology for nanoparticles design and fabrication. Nanoscale 2010;2:1324–47.
[4] Herrmann IK, Grass RN, Mazunin D, Stark WJ. Synthesis and covalent surface functionalization of nonoxidic iron core−shell nanomagnets. Chem Mater 2009;21:3275–81.
[5] Gupta AK, Gupta M. Synthesis and surface engineering of iron oxide nanoparticles for biomedical applications. Biomaterials 2005;26:3995–4021.
[6] Gul S, Khan SB, Rehman IU, Khan MA, Khan MI. A comprehensive review of magnetic nanomaterials modern day theranostics. Front Mater 2019;6. https://doi.org/10.3389/fmats.2019.00179.
[7] Majewski P, Thierry B. Functionalized magnetite nanoparticles—synthesis, properties, and bio-applications. Crit Rev Solid State Mater Sci 2007;32:203–15.
[8] Strobel R, Pratsinis SE. Direct synthesis of maghemite, magnetite and wustite nanoparticles by flame spray pyrolysis. Adv Powder Technol 2009;20:190–4.
[9] Li D, Teoh WY, Selomulya C, Woodward RC, Munroe P, Amal R. Insight into microstructural and magnetic properties of flame-made γ-Fe_2O_3 nanoparticles. J Mater Chem 2007;17:4876.
[10] Jossen R, Pratsinis SE, Stark WJ, Madler L. Criteria for flame-spray synthesis of hollow, shell-like, or inhomogeneous oxides. J Am Ceram Soc 2005;88:1388–93.
[11] Grimm S, Stelzner T, Leuthäußer J, Barth S, Heide K. Particle size effects on the thermal behaviour of maghemite synthesised by flame pyrolysis. Thermochim Acta 1997;300:141–8.
[12] Grimm S, Schulz M, Barth S, Müller R. Flame pyrolysis – a preparation route for ultrafine pure gamma-Fe_2O_3 powders and the control of their particle size and properties. J Mater Sci 1997;32:1083–92.
[13] Alkan B, Medina D, Landers J, Heidelmann M, Hagemann U, Salamon S, Andronescu C, Wende H, Schulz C, Schuhmann W, Wiggers H. Spray-Flame-Prepared $LaCo_{1-x}FexO_3$ perovskite nanoparticles as active OER catalysts: influence of Fe content and low-temperature heating. ChemElectroChem 2020;7:2564–74.
[14] Carvajal L, Buitrago-Sierra R, Santamaría A, Angel S, Wiggers H, Gallego J. Effect of spray parameters in a spray flame reactor during FexOy nanoparticles synthesis. J Therm Spray Tech 2020;29:368–83.
[15] Sorvali M, Honkanen M, Hyvärinen L, Kuisma R, Larjo J, Mäkelä JM. Crystallographic phase formation of iron oxide particles produced from iron nitrate by liquid flame spray with a dual oxygen flow. Int Jnl Ceramic Engine Sci 2021;3:227–36.
[16] Sorvali M, Nikka M, Juuti P, Honkanen M, Salminen T, Hyvärinen L, Mäkelä JM. Controlling the phase of iron oxide nanoparticles fabricated from iron(III) nitrate by liquid flame spray. Int Jnl Ceramic Engine Sci 2019;1:194–205.
[17] Bieber M, Al-Khatib M, Fröde F, Pitsch H, Reddemann MA, Schmid HJ, Tischendorf R, Kneer R. Influence of angled dispersion gas on coaxial atomization, spray and flame formation in the context of spray-flame synthesis of nanoparticles. Exp Fluids 2021;62:1–13.
[18] Schneider F, Suleiman S, Menser J, Borukhovich E, Wlokas I, Kempf A, Wiggers H, Schulz C. SpraySyn—a standardized burner configuration for nanoparticle synthesis in spray flames. Rev Sci Instrum 2019;90:85108.
[19] Aßmann S, Münsterjohann B, Huber FJT, Will S. Droplet sizing in spray flame synthesis using wide-angle light scattering (WALS). Appl Phys B 2020;126:1–13.
[20] Aßmann S, Münsterjohann B, Huber FJT, Will S. *In situ* determination of droplet and nanoparticle size distributions in spray flame synthesis by wide-angle light scattering (WALS). Materials 2021;14:6698 (Basel).
[21] Bierwirth M, Olszok V, Ganesan VA, Poostforooshan J, Weber AP. Investigation of particle formation of electrospray flame pyrolysis using a scanning mobility particle sizer. Chem Ing Tech 2021;93:1307–15.
[22] Foo CT, Unterberger A, Martins FJ, Prenting MM, Schulz C, Mohri K. Investigating spray flames for nanoparticle synthesis via tomographic imaging using multi-simultaneous measurements (TIMes) of emission. Opt Express 2022;30:15524–45.
[23] Karaminejad S, Dupont SM, Bieber M, Reddemann MA, Kneer R, Dreier T, Endres T, Schulz C. Characterization of spray parameters and flame stability in two modified nozzle configurations of the SpraySyn burner. Proc Combust Inst 2023;39:2673–82.
[24] Kumar A, Kirchmann J, Beyrau F, Kronenburg A. Jet flapping and its effect on flame oscillations in the SPP1980 SpraySyn burner. Exper Thermal Fluid Sci 2023;142:110826.
[25] Li H, Riefler N, Wriedt T, Mädler L. Reference data set for three-dimensional measurements of double droplet combustion of p-xylene. Proc Combust Inst 2021;38:3151–8.
[26] Martins FJWA, Kirchmann J, Kronenburg A, Beyrau F. Experimental investigation of axisymmetric, turbulent, annular jets discharged through the nozzle of the SPP1980 SpraySyn burner under isothermal and reacting conditions. Exp Therm Fluid Sci 2020;114.
[27] Prenting MM, Bin Dzulfida MI, Dreier T, Schulz C. Characterization of tracers for two-color laser-induced fluorescence liquid-phase temperature imaging in sprays. Exp Fluids 2020;61:1–15.
[28] Prenting MM, Shilikhin M, Dreier T, Schulz C, Endres T. Characterization of tracers for two-color laser-induced fluorescence thermometry of liquid-phase temperature in ethanol, 2-ethylhexanoic-acid/ethanol mixtures, 1-butanol, and o-xylene. Appl Opt 2021;60:C98–113.
[29] Rahinov I, Sellmann J, Lalanne MR, Nanjaiah M, Dreier T, Cheskis S, Wlokas I. Insights into the mechanism of combustion synthesis of iron oxide nanoparticles gained by laser diagnostics, mass spectrometry, and numerical simulations: a mini-review. Energy Fuels 2020;35:137–60.
[30] Simmler M, Meier M, Nirschl H. Characterization of fractal structures by spray flame synthesis using X-ray scattering. Materials 2022;15:2124 (Basel).
[31] Simmler M, Meier M, Rank L, Buth G, Plech A, Nirschl H. Beamline setup for *in situ* measurements of particles in turbulent spray flames using small angle X-ray scattering. In: Proceedings of the Combustion Institute; 2022. https://doi.org/10.1016/j.proci.2022.08.002.
[32] Stodt M, Wriedt T, Kiefer J, Fritsching U. Theoretical investigation of global rainbow refractometry in spray combustion of polydisperse microdroplets. J Mod Opt 2021;68:259–66.
[33] Stodt MFB, Kiefer J, Fritsching U. Ethanol droplet formation, dynamics and combustion mode in the flame of the SpraySyn-nozzle. Exp Fluids 2019;60:1–11.
[34] Stodt MFB, Kiefer J, Fritsching U. Drop dynamics in heterogeneous spray flames for nanoparticle synthesis. At Sprays 2020;30.
[35] Stodt MFB, Liu C, Li S, Maedler L, Fritsching U, Kiefer J. Phase-selective laser-induced breakdown spectroscopy in flame spray pyrolysis for iron oxide nanoparticle synthesis. Proc Combust Inst 2021;38:1711–8.
[36] Suleiman S, Nanjaiah M, Skenderovic I, Rosenberger T, Kunze F, Wlokas I, Kruis FE, Wiggers H, Schulz C. Atmospheric-pressure particle mass spectrometer for investigating particle growth in spray flames. J Aerosol Sci 2021;158:105827.
[37] Tischendorf R, Simmler M, Weinberger C, Bieber M, Reddemann M, Fröde F, Lindner J, Pitsch H, Kneer R, Tiemann M. Examination of the evolution of iron oxide nanoparticles in flame spray pyrolysis by tailored in situ particle sampling techniques. J Aerosol Sci 2021;154:105722.
[38] Abdelsamie A, Chi C, Nanjaiah M, Skenderović I, Suleiman S, Thévenin D. Direct numerical simulation of turbulent spray combustion in the spraysyn burner: impact of injector geometry. Flow Turbul Combust 2021;106:453–69.
[39] Abdelsamie A, Kruis FE, Wiggers H, Thévenin D. Nanoparticle formation and behavior in turbulent spray flames investigated by DNS. Flow Turbul Combust 2020;105:497–516.
[40] Abdelsamie A, Thévenin D. On the behavior of spray combustion in a turbulent spatially-evolving jet investigated by direct numerical simulation. Proc Combust Inst 2019;37:3373–82.
[41] F. Fröde, T. Grenga, S.M. Dupont, R. Kneer, R. Tischendorf, O. Massopa, H.J. Schmid, H. Pitsch, Large eddy simulation of iron oxide formation in a laboratory spray flame (2023).
[42] Kirchmann J, Kronenburg A, Stein OT, Cleary MJ. Two-phase sparse-Lagrangian MMC-LES of dilute ethanol spray flames. Proc Combust Inst 2021;38:3343–50.
[43] Kotalczyk G, Skenderović I, Kruis FE. Monte Carlo simulations of homogeneous nucleation and particle growth in the presence of background particles. Tellus B Chem Phys Meteorol 2019;71:1554415.
[44] Martins FJWA, Kirchmann J, Kronenburg A, Beyrau F. Quantification and mitigation of PIV bias errors caused by intermittent particle seeding and particle lag by means of large eddy simulations. Meas Sci Technol 2021;32:104006.
[45] Nanjaiah M, Pilipodi-Best A, Lalanne MR, Fjodorow P, Schulz C, Cheskis S, Kempf A, Wlokas I, Rahinov I. Experimental and numerical investigation of iron-doped flames: feO formation and impact on flame temperature. Proc Combust Inst 2021;38:1249–57.
[46] Saber F, Abdelsamie A, Sedrak M. Numerical investigation of particle spray size distribution in turbulent jet flow. J Eng Res 2022;174:M19–40.
[47] Sellmann J, Wollny P, Baik SJ, Suleiman S, Schneider F, Schulz C, Wiggers H, Wlokas I, Kempf AM. LES of nanoparticle synthesis in the spraysyn burner: a comparison against experiments. Powder Technol 2022;404:117466.
[48] Skenderović I, Kotalczyk G, Kruis FE. Dual population balance Monte Carlo simulation of particle synthesis by flame spray pyrolysis. Processes 2018;6:253.
[49] Wollny P, Angel S, Wiggers H, Kempf AM, Wlokas I. Multiscale simulation of the formation of platinum-particles on alumina nanoparticles in a spray flame experiment. Fluids 2020;5:201.
[50] Strobel R, Pratsinis SE. Effect of solvent composition on oxide morphology during flame spray pyrolysis of metal nitrates. Phys Chem Chem Phys 2011;13:9246–52.
[51] Goudeli E, Gröhn AJ, Pratsinis SE. Sampling and dilution of nanoparticles at high temperature. Aerosol Sci Technol 2016;50:591–604.
[52] Gröhn AJ, Eggersdorfer ML, Pratsinis SE, Wegner K. On-line monitoring of primary and agglomerate particle dynamics. J Aerosol Sci 2014;73:1–13.

[53] Stodt MFB, Gonchikzhapov M, Kasper T, Fritsching U, Kiefer J. Chemistry of iron nitrate-based precursor solutions for spray-flame synthesis. Phys Chem Chem Phys 2019;21:24793–801.
[54] Keller A, Wlokas I, Kohns M, Hasse H. Thermophysical properties of solutions of Iron (III) nitrate-nonahydrate in mixtures of ethanol and water. J Chem Eng Data 2020;65:3519–27.
[55] Meierhofer F, Li H, Gockeln M, Kun R, Grieb T, Rosenauer A, Fritsching U, Kiefer J, Birkenstock J, Mädler L, Pokhrel S. Screening precursor-solvent combinations for $Li_4Ti_5O_{12}$ energy storage material using flame spray pyrolysis. ACS Appl Mater Interfaces 2017;9:37760–77.
[56] Angel S, Schneider F, Apazeller S, Kaziur-Cegla W, Schmidt TC, Schulz C, Wiggers H. Spray-flame synthesis of $LaMO_3$ (M= Mn, Fe, Co) perovskite nanomaterials: effect of spray droplet size and esterification on particle size distribution. Proc Combust Inst 2021;38:1279–87.
[57] Angel S, Neises J, Dreyer M, Friedel Ortega K, Behrens M, Wang Y, Arandiyan H, Schulz C, Wiggers H. Spray-flame synthesis of La(Fe, Co)O_3 nano-perovskites from metal nitrates. AIChE J 2020;66. https://doi.org/10.1002/aic.16748.
[58] Angel S, Tapia JD, Gallego J, Hagemann U, Wiggers H. Spray-flame synthesis of LaMnO 3+δ nanoparticles for selective CO Oxidation (SELOX). Energy Fuels 2021; 35:4367–76.
[59] Stefanidis EK, Ebaugh TA, Bliznakov S, Bonville LJ, Maric R, Carbone F. Laser diagnostics to characterize the in-flame growth of platinum nanoparticles manufactured by the reactive spray deposition technology. Combust Flame 2022; 246:112412.
[60] Cornell RM, Schwertmann U. The iron oxides: structure, properties, reactions, occurrences, and uses. others. Wiley-vch Weinheim; 2003.
[61] Schwertmann U, Cornell RM. Iron oxides in the laboratory: preparation and characterization. John Wiley & Sons; 2008.
[62] Hanesch M. Raman spectroscopy of iron oxides and (oxy)hydroxides at low laser power and possible applications in environmental magnetic studies. Geophys J Int 2009;177:941–8.
[63] Debye P, Scherrer P. Interference on inordinate orientated particles in roentgen light. Phys Z 1916;17:277–83.
[64] Brunauer S, Emmet PH, Teller E. Adsorption of gases in multimolecular layers. J Am Chem Soc 1938;60:309–19.
[65] Maricq M, Harris SJ, Szente JJ. Soot size distributions in rich premixed ethylene flames. Combust Flame 2003;132:328–42.
[66] Maricq MM. Size and charge of soot particles in rich premixed ethylene flames. Combust Flame 2004;137:340–50.
[67] Kasper M, Siegmann K, Sattler K. Evaluation of an *in situ* sampling probe for its accuracy in determining particle size distributions from flames. J Aerosol Sci 1997; 28:1569–78.
[68] de Filippo A, Sgro LA, Lanzuolo G, D'Alessio A. Probe measurements and numerical model predictions of evolving size distributions in premixed flames. Combust Flame 2009;156:1744–54.
[69] de Filippo A, Sgro LA, Alessio AD. Sampling and analysis system to collect and measure nanoparticle size distribution produced in ethylene-air flame. In: 29th Meeting on Combustion Italian Section of the Combustion Institute; 2006.
[70] Zhao B, Yang Z, Wang J, Johnston MV, Wang H. Analysis of soot nanoparticles in a laminar premixed ethylene flame by scanning mobility particle sizer. Aerosol Sci Technol 2003;37:611–20.
[71] Carbone F, Attoui M, Gomez A. Challenges of measuring nascent soot in flames as evidenced by high-resolution differential mobility analysis. Aerosol Science and Technology 2016;50:740–57.
[72] Mätzing H, Vlavakis P, Trimis D, Stapf D. A computational fluid dynamics study of flame gas sampling in horizontal dilution tubes. Flow 2022;2. https://doi.org/10.1017/flo.2022.10.
[73] de Faria DLA, Silva SV, de Oliveira MT. Raman microspectroscopy of some iron oxides and oxyhydroxides. J Raman Spectrosc 1997;28:873–8.
[74] Jubb AM, Allen HC. Vibrational spectroscopic characterization of hematite, maghemite, and magnetite thin films produced by vapor deposition. ACS Appl Mater Interfaces 2010;2:2804–12.
[75] Oh SJ, Cook DC, Townsend HE. Characterization of iron oxides commonly formed as corrosion products on steel. Hyperfine Interact 1998;112:59–66.
[76] Sklute EC, Kashyap S, Dyar MD, Holden JF, Tague T, Wang P, Jaret SJ. Spectral and morphological characteristics of synthetic nanophase iron (oxyhydr)oxides. Phys Chem Miner 2018;45:1–26.
[77] Dar MI, Shivashankar SA. Single crystalline magnetite, maghemite, and hematite nanoparticles with rich coercivity. RSC Adv 2014;4:4105–13.
[78] Zoppi A, Lofrumento C, Castellucci EM, Migliorini MG. The Raman spectrum of hematite: possible indicator for a compositional or firing distinction among Terra Sigillata wares. Ann Chim 2005;95:239–46.
[79] Lee YJ, Jun KW, Park JY, Potdar HS, Chikate RC. A simple chemical route for the synthesis of γ-Fe_2O_3 nano-particles dispersed in organic solvents via an iron–hydroxy oleate precursor. J Ind Eng Chem 2008;14:38–44.
[80] Rémazeilles C, Refait P. Fe(II) hydroxycarbonate $Fe_2(OH)_2CO_3$ (chukanovite) as iron corrosion product: synthesis and study by Fourier transform infrared spectroscopy. Polyhedron 2009;28:749–56.
[81] Huu Do BP, Nguyen BD, Nguyen HD, Nguyen PT. Synthesis of magnetic composite nanoparticles enveloped in copolymers specified for scale inhibition application. Adv Nat Sci 2013;4:45016.
[82] Bargar JR, Kubicki JD, Reitmeyer R, Davis JA. ATR-FTIR spectroscopic characterization of coexisting carbonate surface complexes on hematite. Geochim Cosmochim Ac 2005;69:1527–42.
[83] Wlasits PJ, Stolzenburg D, Tauber C, Brilke S, Schmitt SH, Winkler PM, Wimmer D. Counting on chemistry: laboratory evaluation of seed-material-dependent detection efficiencies of ultrafine condensation particle counters. Atmos Meas Tech 2020;13:3787–98.
[84] Liu Y, Attoui M, Li Y, Chen J, Li Q, Wang L. Factors that govern sub-3nm particle measurements in an Airmodus ® PSM and a TSI ® DEG–SMPS. Aerosol Sci Technol 2022;56:883–92.
[85] Eggersdorfer ML, Pratsinis SE. Restructuring of aggregates and their primary particle size distribution during sintering. AIChE J 2013;59:1118–26.
[86] Eggersdorfer ML, Pratsinis SE. Agglomerates and aggregates of nanoparticles made in the gas phase. Adv Powder Technol 2014;25:71–90.
[87] Goudeli E, Eggersdorfer ML, Pratsinis SE. Coagulation-agglomeration of fractal-like particles: structure and self-preserving size distribution. Langmuir 2015;31: 1320–7.
[88] Sorensen CM. The mobility of fractal aggregates: a review. Aerosol Sci Technol 2011;45:765–79.
[89] Vemury S, Kusters KA, Pratsinis SE. Time-lag for attainment of the self-preserving particle size distribution by coagulation. J Colloid Interface Sci 1994;165:53–9.
[90] Vemury S, Pratsinis SE. Self-preserving size distributions of agglomerates. J Aerosol Sci 1995;26:175–85.
[91] Carbone F. Probing gas-to-particle transition in a moderately sooting atmospheric pressure ethylene/air laminar premixed flame. part ii: molecular clusters and nascent soot particle size distributions. Combust Flame 2007.
[92] Raj A, Sander M, Janardhanan V, Kraft M. A study on the coagulation of polycyclic aromatic hydrocarbon clusters to determine their collision efficiency. Combust Flame 2010;157:523–34.
[93] TSI Incorporated, aerosol instrument manager software for scanning mobility particle sizer (SMPS) spectrometers (2022).
[94] Tigges L, Wiedensohler A, Weinhold K, Gandhi J, Schmid HJ. Bipolar charge distribution of a soft X-ray diffusion charger. J Aerosol Sci 2015;90:77–86.
[95] Tauber C, Steiner G, Winkler PM. Counting efficiency determination from quantitative intercomparison between expansion and laminar flow type condensation particle counter. Aerosol Sci Technol 2019;53:344–54.
[96] Hermann M, Wehner B, Bischof O, Han HS, Krinke T, Liu W, Zerrath A, Wiedensohler A. Particle counting efficiencies of new TSI condensation particle counters. J Aerosol Sci 2007;38:674–82.
[97] Tsantilis S, Pratsinis SE. Soft- and hard-agglomerate aerosols made at high temperatures. Langmuir 2004;20:5933–9.
[98] Dobbins RA, Megaridis CM. Morphology of flame-generated soot as determined by thermophoretic sampling. Langmuir 1987;3:254–9.